IEEE Access
Multidisciplinary | Rapid Review | Open Access Journal

Received June 22, 2019, accepted July 9, 2019, date of publication July 16, 2019, date of current version August 5, 2019.

Digital Object Identifier 10.1109/ACCESS.2019.2929122

An Improved Accurate Solver for the Time-Dependent RTE in Underwater Optical Wireless Communications

ELMEHDI ILLI[1], (Student Member, IEEE), FAISSAL EL BOUANANI[1], (Member, IEEE), KI-HONG PARK[2], (Member, IEEE), FOUAD AYOUB[3], (Member, IEEE), AND MOHAMED-SLIM ALOUINI[2], (Fellow, IEEE)

[1]ENSIAS College of Engineering, Mohammed V University, Rabat 10000, Morocco
[2]Computer, Electrical, and Mathematical Sciences and Engineering (CEMSE) Division, King Abdullah University of Science and Technology (KAUST), Thuwal 23955-6900, Saudi Arabia
[3]CRMEF, Kenitra 14000, Morocco

Corresponding author: Faissal El Bouanani (f.elbouanani@um5s.net.ma)

This work was supported by the Office of Sponsored Research (OSR), KAUST.

ABSTRACT Underwater optical wireless communication (UOWC) has been widely advocated as a viable way to satisfy these high-speed links constraints in the marine medium through the use of the visible spectrum. Nevertheless, UOWC faces several limitations, such as the path-loss due to the absorption and scattering phenomena, caused by underwater particles. Thus, quantifying this path-loss is of paramount importance in the design of futuristic UOWC systems. To this end, several approaches have been used in this regard, namely the Beer–Lambert's law, Monte Carlo simulation, as well as radiative transfer equation (RTE). This last mentioned evaluates the optical path-loss of the light wave in an underwater channel in terms of the absorption and scattering coefficients as well as the scattering phase function (SPF). In this paper, an improved numerical solver to evaluate the time-dependent RTE for UOWC is proposed. The proposed numerical algorithm was improved based on the previously proposed ones, by making use of an improved finite difference scheme, a modified scattering angular discretization, as well as an enhancement of the quadrature method by involving a more accurate seven-point quadrature scheme in order to calculate the weight coefficients corresponding to the RTE integral term. Importantly, we applied the RTE solver to three different volume scattering functions, namely the single-term Henyey–Greenstein (HG) phase function, the two-term HG phase function, and the Fournier–Forand phase function, over both Harbor-I and Harbor-II water types. Based on the normalized received power evaluated through the proposed algorithm, the bit error rate performance of the UOWC system is investigated in terms of system and channel parameters. The enhanced algorithm gives a tightly close performance to its Monte Carlo counterpart by adjusting the numerical cumulative distribution function computation method as well as optimizing the number of scattering angles.

INDEX TERMS Absorption, finite difference equation, inherent optical properties, numerical resolution, phase scattering functions, quadrature method, radiative transfer equation (RTE), scattering, underwater optical wireless communication (UOWC).

I. INTRODUCTION

With the prospering of the wireless communication industry over the last decades, human exploration in the underwater environment increased significantly. More recently, a notable increase in research activities in the marine medium has been witnessed, which enabled the deployment of ocean exploration and communication systems [1], [2]. Throughout the last few years, the scientific community have witnessed the emergence of various underwater applications, which have attracted much attention, such as climate recording, ecological monitoring, oil production control, and military surveillance [3]. With this permanent emphasis on researches in the marine medium, underwater wireless sensors network

The associate editor coordinating the review of this manuscript and approving it for publication was Gurkan Tuna.

concept evolved remarkably, so as to enable the concretization of several critical commercial and military applications and services [4]. In particular, wireless communication nodes such as wireless sensors, floating buoys, and submarines require reliable links with higher data rates in order to fulfill communication requirements and exchange a relatively huge amount of data [5].

Optical wireless communication (OWC) is an emerging technology that received considerable attention lastly, as a promising key-enabling technology for high-speed terrestrial and underwater communications [3]. It consists of transmitting the information signals in the form of light conical beams using LED or laser devices through either the free space; i.e. visible light communication (VLC), free space optics (FSO), or the underwater medium (UOWC) [6], [7]. Due to its great potential for providing a tremendous amount of bandwidth, high security as well as immunity to interference, OWC is the most advocated solution in providing a low-latency communication link with data rates of tens of Gbps over moderate distances [8].

Generally, light propagation in the marine medium is corrupted by three main phenomena: Stochastic phenomena, namely (i) turbulence-induced fading due to sea movement as well as temperature and pressure inhomogeneities [3], (ii) pointing errors due to transceiver motion [2]. On the other hand, (iii) path-loss is a deterministic phenomenon affecting light propagation caused mainly by photons absorption and scattering, representing the two major inherent optical properties (IOP) that quantify light power loss [9]. Absorption is the process where the photons lose their energy by conversion into another form such as chemical or heat, while scattering indicates the photons direction change due to the light interaction with the medium particles and molecules [9]. That is, the greater the scattering and absorption coefficients, the severer the power loss in the medium.

Several approaches in the literature have been proposed to analyze and predict the total light power path-loss in the marine medium. Beer-Lambert's law is a deterministic approach, and it is the simplest model applied to evaluate the optical loss [2]. Indeed, it considers an exponential decay of the received light intensity as a function of the propagation distance, attenuation coefficient, defined as the sum of absorption and scattering coefficients, as well as source intensity. However, its main drawback lies in assuming that the scattered photons are completely lost, while in fact, some of them can still be captured at the receiver after multiple scattering, and therefore the received power is underestimated [10]. On the other hand, Monte Carlo simulation method is among popular numerical approaches to evaluate the optical path loss in underwater medium. It is a probabilistic method that emulates underwater light transmission loss by transmitting and tracking the propagation of a huge number of simulated photons [11], [12]. Its main benefits lie in its easy implementation in computation platforms, as well as its acceptable accuracy often. However, its main limitation lies in the errors related to the random values generators as well as its long-running time [2].

Within the past few years, the use of radiative transfer equation (RTE) has attracted significant attention in the fields of optics for biomedical imaging [13]. In particular, it is considered as a deterministic solution for describing light propagation in multiple absorbing and scattering medium (e.g., fluids, underwater environment), in terms of the medium IOP, such as absorption and scattering coefficients as well as the scattering phase function (SPF). Interestingly, this last-mentioned defines the scattering power distribution over the various directions in the propagation medium. In this regard, the single-term Henyey-Greenstein (STHG) function has been widely adopted as an analytical model for highly peaked forward scattering environments [10]. Nevertheless, due to the inaccurate fitting of the STHG phase function with scattering measurements for most of the realistic marine environments, the two-terms Henyey-Greenstein (TTHG) and the Fournier-Forand (FF) phase functions have been advocated as analytical models for the underwater SPF modeling.

Even though the RTE is already more than a century old, very few works along this period involved this equation for evaluating the light power loss in various scattering mediums, since it is enough complicated to solve the integro-differential RTE analytically. Actually, various numerical approaches have been used for this purpose, namely [10], [14], [15], and [16]. In [14], a numerical approach to solve the time-dependent (TD) RTE using the finite difference equation and the discrete ordinate method (DOM) was proposed. This last-mentioned consists of discretizing the angular and spatial coordinates uniformly into finite equally spaced points. Interestingly, trapeze quadrature method was used to solve the RTE integral term. The authors in [15] deployed another numerical approach for solving the steady-state time-independent (TI) RTE, based also on the DOM and the upwind finite difference scheme for the partial derivatives, as well as using the 3-points Simpson's quadrature method to solve the integral term. In [10], an improvement was made related to the numerical proposal in [15], where an optimal non-uniform angular discretization through the Lloyd-Max algorithm [17] is proposed. Furthermore, the Gauss-Seidel iterative method was involved to solve the fully discretized system of linear equations. Finally, the proposed solver in [10] was improved in [16] by involving a two-neighbors derivative for space coordinates in addition to involving time derivative, as well as incorporating the 5-points quadrature scheme alongside with the 3-points one. It is noteworthy that the majority of the previous related works dealt with the STHG as an SPF.

In this paper, an enhancement of the numerical TD-RTE solvers developed in [10] and [16] is investigated. Distinctly to these aforementioned solvers where the 3 and 5-points quadrature schemes were applied to neighbor scattering angles, which is inaccurate, we involve in this paper the 7-points quadrature scheme, which we apply to infinitesimally small subintervals. Additionally, the scattering angles

discretizing algorithm used in the two aforementioned works was modified. The main contributions of this paper are highlighted as follows:

- The 3 and 5-points quadrature methods used in [10] and [16], respectively, are adjusted by involving the 7-points rule given by the Newton-Cotes formula. The quadrature method aims at determining the weight coefficients in order to compute the integral term of the TD-RTE. Distinctly from [10] and [16], where the above-mentioned quadrature schemes were applied to neighboring scattering angles, which is an inaccurate approach since the step between two angles is relatively great, we propose to apply this interpolation method to the discretized infinitesimally small subintervals within the interval between two successive scattering angles.
- Distinctly from [10] and [16], the mean squared error (MSE) based algorithm, used for the scattering angles discretization, is modified. In particular, the updated version in this paper relaxes the symmetric scattering distribution considered previously. Furthermore, the receiver's field of view (FOV) has been discretized in a similar manner to the scattering angles.
- As performed in [16], a more accurate finite upwind difference scheme, incorporating two neighbor points, is involved.
- In addition to applying the TD-RTE solver to the classical STHG function used in [10] and [16], the TTHG and FF phase functions are also adopted as SPFs in this work.
- Monte Carlo simulation provided in [11] was updated, by modifying the numerical cumulative distribution function (CDF) computation as well as optimizing the number of generated scattering angles for each subinterval of two successive distances.
- The bit error rate (BER) performance is analyzed, based on the evaluated received power, as a function of propagation time and distance as well as the system and channel parameters.
- The numerical RTE results are compared with their Monte Carlo (MC) counterparts, performed based on the proposed simulation algorithm in [11]. Furthermore, the proposed numerical RTE solver and MC simulation complexities are compared in terms of computation time.
- Matlab codes for the developed RTE Solver are presented at the end of the paper [18].

In this context, the remainder of this paper is organized as follows: Section II presents the UOWC system model as well as the improved TD-RTE solver. A numerical application of the derived results is shown in Section III. Section IV concludes the paper with some future directions.

II. SYSTEM MODEL

The light propagation on the three-dimensional space is affected mainly by two main phenomena: (i) Absorption by which the photon energy is converted into another form, (ii) and scattering is described as the light interaction with the medium particles and molecules. As depicted in Fig. 1, the incident power P_I, propagating toward the direction $\vec{n}$, undergoes absorption and scattering in a volume element ΔV with width Δr, with P_A and P_S denote the absorbed and scattered amounts of power within ΔV, respectively. A portion of the incident power, denoted P_T, will conserve the propagation direction of the incident wave. Following the energy-conservation law, one obtains

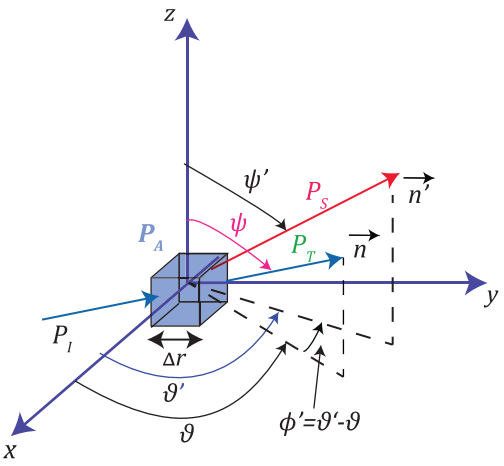

FIGURE 1. Light propagation in the three-dimensional space.

$$P_I = P_A + P_S + P_T. \tag{1}$$

The wavelength-dependent absorption and scattering coefficients, measured in m^{-1}, are defined as [2]

$$a(\lambda) = \lim_{\Delta r \to 0} \frac{P_A}{\Delta r P_I}, \tag{2}$$

and

$$b(\lambda) = \lim_{\Delta r \to 0} \frac{P_S}{\Delta r P_I}, \tag{3}$$

where λ being the operating wavelength. The total attenuation coefficient $c(\lambda)$, measured in m^{-1}, is defined as the sum of the absorption and scattering ones as

$$c(\lambda) = a(\lambda) + b(\lambda). \tag{4}$$

In the sequel, we will assume a fixed wavelength. Thus, the absorption, scattering, and attenuation coefficients are fixed.

It is known that the instantaneous light radiance is the solution of the three-dimensional TD-RTE given as [9], [14]

$$\left[\frac{1}{v}\frac{\partial}{\partial t} + \vec{n} \cdot \nabla\right] L(t, r, \vartheta, \Psi) = -cL(t, r, \vartheta, \Psi) + S(t) + \int_{\vartheta'=0}^{2\pi} \int_{\Psi'=0}^{\pi} \beta(\vartheta, \Psi, \vartheta', \Psi') \times L(t, r, \vartheta', \Psi') \sin(\Psi') \, d\Psi' d\vartheta', \tag{5}$$

where

- $L(t, r, \vartheta, \Psi)$ denotes the light radiance at position r from the source, and at time t propagating toward direction $\overrightarrow{n}$ in $W/m^2/sr$. It is defined as the amount of power at distance r and time t, per unit of surface and per unit of solid angle.
- $S(t)$ being the directed light source radiance at time t in $W/m^3/sr$. It is defined as the radiated power density per unit of volume per unit of solid angle.
- $\beta\left(\Psi, \vartheta, \Psi', \vartheta'\right)$ is the volume scattering function (VSF), representing the probability density function (PDF) of the scattered power between two directions $\overrightarrow{n}$ and $\overrightarrow{n}'$, represented by the angles (Ψ, ϑ) and $\left(\Psi', \vartheta'\right)$, respectively.
- ∇ is the divergence operator.
- v being the light celerity in the underwater medium.

Remark 1: In the sequel, we will consider the 2D VSF $\beta\left(\vartheta, \vartheta'\right)$. That is, the RTE will be solved in two dimensions rather than 3D. Consequently, the considered optical radiances are measured in $W/m^2/rad$. In this case, the double integral over the solid angle of a sphere, given in (5), will be replaced by a simple integral of ϑ' argument over $[0, 2\pi]$, when $\Psi' = \frac{\pi}{2}$. Consequently, the 2D RTE equation is expressed as

$$\left[\frac{1}{v}\frac{\partial}{\partial t} + \overrightarrow{n} \cdot \nabla\right] L(t, r, \vartheta) = -cL(t, r, \vartheta) + \int_0^{2\pi} \beta\left(\vartheta, \vartheta'\right) \times L\left(t, r, \vartheta'\right) d\vartheta' + S(t), \quad (6)$$

The VSF $\beta\left(\vartheta, \vartheta'\right)$ is related to the SPF $\widetilde{\beta}\left(\phi'\right)$ as [2]

$$\beta\left(\vartheta, \vartheta'\right) = b\widetilde{\beta}\left(\phi'\right), \quad (7)$$

where ϕ' denotes the scattering angle between the two directions $\overrightarrow{n}$ and $\overrightarrow{n}'$.

The scalar product of the scattering vector $\overrightarrow{n}'$ with unit vectors $\overrightarrow{e}_x$, $\overrightarrow{e}_y$ is given by, respectively

$$\overrightarrow{n}' \cdot \overrightarrow{e}_x = \cos\vartheta', \quad (8)$$

$$\overrightarrow{n}' \cdot \overrightarrow{e}_y = \sin\vartheta', \quad (9)$$

where ϑ and ϑ' are defined as the angles between the x-axis and the propagation and scattering vectors $\overrightarrow{n}$ and $\overrightarrow{n}'$ in the XOY plane, respectively.

A. SINGLE TERM HG FUNCTION

A popular analytical model for representing anisotropic propagation of light is the two-dimensions (2D) single term Henyey-Greenstein (STHG) SPF given as [15]

$$\widetilde{\beta}_{STHG}\left(g, \phi'\right) = \frac{1 - g^2}{2\pi\left(1 + g^2 - 2g\cos\phi'\right)}, \quad 0 \le g \le 1, \quad (10)$$

where g accounts for the scattering strength, i.e., isotropic scattering is defined for $g = 0$, while as g tends to 1, a peaked scattering scenario is presented. Interestingly, it has been shown that the value $g = 0.93$ represents an accurate approximation for the angular distribution of scattered light in the majority of water types [2]. The backscattering ratio, defined as the fraction of light scattered in the backward direction out of the total scattered light, can be expressed for the STHG SPF in terms of scattering strength g as [19]

$$B_p = \frac{1 - g}{2g}\left(\frac{1 + g}{\sqrt{1 + g^2}} - 1\right). \quad (11)$$

B. TWO TERMS HG FUNCTION

Due to the inaccurate fitting of the STHG phase function with measurements at small and large scattering angles, a linear combination of Henyey-Greenstein phase functions is sometimes used to improve the fit at small and large angles. The TTHG phase function is given as [20]

$$\widetilde{\beta}_{TTHG}\left(\alpha, g_1, g_2, \phi'\right) = \alpha\widetilde{\beta}_{STHG}\left(g_1, \phi'\right) + (1 - \alpha)\widetilde{\beta}_{STHG}\left(g_2, \phi'\right), \quad (12)$$

where g_1 and g_2 stands for scattering strength parameters related to the STHG SPF, over the forward and backward scattering angles, respectively [20], and α is a weighting factor between 0 and 1, representing the relative contribution of the forward and backward scattering terms. The relationship between the abovementioned parameters and the backscattering ratio B_p is given as

$$g_2 = -0.30614 + 1.0006g_1 - 0.01826g_1^2 + 0.03644g_1^3, \quad (13)$$

$$\alpha = \frac{g_2\left(1 + g_2\right)}{\left(g_1 + g_2\right)\left(1 + g_2 - g_1\right)}, \quad (14)$$

$$B_p = \frac{1 + g_2 - \alpha\left(g_1 + g_2\right)}{2 + \frac{\alpha}{2}\left(g_1 + g_2\right) - \frac{g_2}{2}}. \quad (15)$$

C. FOURNIER-FORAND FUNCTION

The Fournier-Forand (FF) function is among other SPFs that have been proposed as an alternative to the STHG and TTHG, in hydraulic optics as well as in underwater optical environments [9]. The two parameters FF phase function, introduced in [21], has a more complex analytical form compared to its STHG and TTHG counterparts. Nevertheless, it depends only on two parameters and has higher accuracy into modeling quasi all realistic underwater phase functions. The FF SPF is expressed as [21], [22]

$$\widetilde{\beta}_{FF}\left(\mu, n_p, \phi'\right) = \left[\begin{array}{l}\left[\delta\left(1 - \delta^{\upsilon}\right) - \upsilon\left(1 - \delta\right)\right]\sin^{-2}\left(\frac{\phi'}{2}\right) \\ +\upsilon\left(1 - \delta\right) - \left(1 - \delta^{\upsilon}\right)\end{array}\right] \times \frac{1}{4\pi(1 - \delta)^2\delta^{\upsilon}} + \frac{1 - \delta_{\pi}^{\upsilon}}{16\pi\left(\delta_{\pi} - 1\right)\delta_{\pi}^{\upsilon}} \times \left(3\cos^2\left(\phi'\right) - 1\right), \quad (16)$$

where n_p is the real refraction index, and μ denotes is the slope parameter of the hyperbolic distribution, with $3 \le \mu \le 5$, and

$$\upsilon = \frac{3 - \mu}{2}, \quad (17)$$

$$\delta = \frac{4}{3(n_p - 1)^2}\sin^2\left(\frac{\phi'}{2}\right), \quad (18)$$

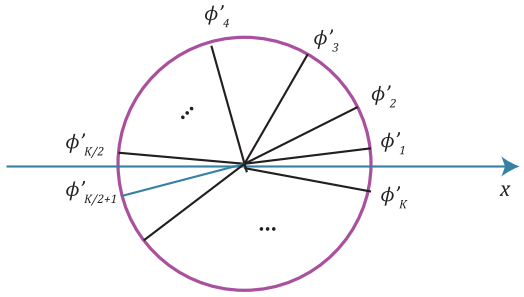

FIGURE 2. Non-uniform scattering directions discretization.

with δ_z being δ evaluated at $\phi' = z$. B_p for the FF SPF can be expressed as

$$B_p = 1 - \frac{1 - \delta_{\pi/2}^{\upsilon+1} - 0.5\left(1 - \delta_{\pi/2}^{\upsilon}\right)}{\delta_{\pi/2}^{\upsilon}\left(1 - \delta_{\pi/2}\right)}. \tag{19}$$

D. OPTIMAL SCATTERING ANGLES: IMPROVED ALGORITHM

In [15], the authors used the uniform discrete ordinate method, based on discretizing the angular space of propagation into discrete equidistant directions. However, this approach seems accurate only for isotropic scattering environments ($g = 0$) and presents some inaccuracies for highly peaked forward scattering waters [1], [10]. Considering the TTHG and FF functions in addition to the STHG one, where the angular directions of light propagation range in the interval $[0, 2\pi]$, the angular space is discretized into K unequally spaced directions ϕ'_k, as shown in Fig. 2, minimizing the following mean squared error [10]

$$f(K) = \sum_{k=1}^{K} \int_{d_{k-1}}^{d_k} \left(\phi'_k - \phi'\right)^2 \widetilde{\beta}_X\left(\Omega, \phi'\right) d\phi', \tag{20}$$

where d_k denote the decision thresholds, X denotes either *STHG*, *TTHG*, or *FF*, while $\left(\Omega, \phi'\right)$ denotes either $\left(g, \phi'\right)$, $\left(\alpha, g_1, g_2, \phi'\right)$, or $\left(\mu, n_p, \phi'\right)$, respectively.

In order to minimize the MSE of the above function, we must satisfy the two following conditions

$$d_k = \frac{\phi'_k + \phi'_{k+1}}{2}; \quad 1 \le k \le K, \tag{21}$$

$$\phi'_k = \frac{\int_{d_{k-1}}^{d_k} \phi' \widetilde{\beta}_X\left(\Omega, \phi'\right) d\phi'}{\int_{d_{k-1}}^{d_k} \widetilde{\beta}_X\left(\Omega, \phi'\right) d\phi'}; \quad 1 \le k \le K. \tag{22}$$

The non-uniform scattering angle discretization process is depicted in Algorithm 1. As a first step of the algorithm, the scattering angles are initialized by a uniform sampling in the $[0, 2\pi]$ interval on K discrete directions, in order to evaluate the thresholds d_k in the first iteration as shown in (21). Then, for a given SPF among the three aforementioned in (10)-(16), new values of d_k are computed at each iteration using (21), based on which ϕ'_k values are updated using (22). The process is iterated until reaching optimal ϕ'_k values.

Algorithm 1 Optimal Scattering Angles

Data: K, g, α, g_1, g_2, μ, n_p, ϵ, SPF
Result: ϕ'_k
begin
- Initialize ϕ'_k uniformly, i.e., $\phi_k'^{(0)} = (k-1)\frac{2\pi}{K}$, $1 \le k \le K$;
- Setting $d_0 = 0$;
- $l \leftarrow 0$;

if *SPF="STHG"* **then**
$\Omega \leftarrow g$;
end
else if *SPF="TTHG"* **then**
$\Omega \leftarrow \alpha, g_1, g_2$;
end
else
$\Omega \leftarrow \mu, n_p$;
end

repeat
- Computing d_k for $1 \le k \le K$ using (21);
- Calculating the new values $\phi_k'^{(l+1)}$ using (10), (12), (16), and (22), for $1 \le k \le K$;
- $l \leftarrow l + 1$;

until $\phi_k'^{(l+1)} - \phi_k'^{(l)} < \epsilon$;
end

In this paper, the Lloyd-Max algorithm, used in [10] and [16] that provides optimal angles through MSE criteria was modified. The angular discretization in the former version was symmetric with respect to the reference forward direction $\left(\phi'_1 = 0\right)$, while in this updated one, the angular discretization is asymmetric with respect to the x-axis. The reference forward direction ϕ'_1 is chosen as $\phi'_1 \neq 0$, which is more practical as the source beam diverges through a divergent lens, by an initial divergence half-angle of ω. That is, K angles will be computed in this version instead of $\frac{K}{2}$, performed in the former one.

The time coordinate is discretized uniformly into equidistant time instants t_n $(1 \le n \le N)$, Δt denotes the discretization step between two consecutive time instants t_n and t_{n+1}, while N accounts for the maximal number of time instants, at which the convergence of the TD-RTE solution is attained.

By discretizing (8) and (9), and plugging them as well as the time discretization into (6), one obtains

$$\eta_k \frac{\partial L_k(t_n, r)}{\partial y} + \xi_k \frac{\partial L_k(t_n, r)}{\partial x} + \frac{1}{v}\frac{\partial L_k(t_n, r)}{\partial t} = -cL_k(t_n, r) + b\sum_{k_s=1}^{K} w_{k,k_s} L_{k_s}(t_n, r) + S(t_n), \quad k = 1, \ldots, K, \; n = 1, \ldots, N, \tag{23}$$

with

- $L_k(t_n, r)$ being the time-dependent radiance at position r propagating toward discrete direction ϕ'_k.

- $\xi_k = \cos\phi'_k$,
- $\eta_k = \sin\phi'_k$.
- w_{k,k_s} denotes the weight terms that substitute the integral term, with k and k_s correspond to the discrete angles of propagation and scattering directions, respectively.

It is worth mentioning that the coefficients w_{k,k_s} in the equation above are obtained through quadrature method, detailed in the next subsection.

E. ACCURATE COMPUTATION OF THE INTEGRAL TERM

In this subsection, in order to solve numerically the integral on the right-hand side of (6), we incorporate the Simpson's method alongside with the 5-points and 7-points Boole's rule given by the Newton-Cotes formulas [23, Eqs. (25.4.14), (25.4.18)], in order to calculate the weight terms w_{k,k_s} given as

$$w_{1,k_s} = \sum_{l=1}^{M} S_{k_s}(l); \quad 1 \le k_s \le K, \tag{24}$$

where $S_{k_s}(l)$ is defined in (25), as shown at the bottom of the next page, $h_{k_s} = \frac{\Delta\phi'_{k_s}}{M}$ denotes an infinitesimally small quadrature discretization step, $\Delta\phi'_{k_s}$ is the difference between the angles ϕ'_{k_s} and ϕ'_{k_s+1}, and M is the number of discrete points within this area, assumed to be the same for all subintervals of scattering angles. $\widetilde{\beta}_X\left(\Omega, \phi'\right)$ is the PDF of the scattered photons, its integration over 2π equals 1. Then, it follows from the equation above that all the terms w_{1,k_s} should be normalized by $\sum_{k_s=1}^{K} w_{1,k_s}$. The remaining terms w_{k,k_s} can be calculated using the formula [10]

$$w_{k,k_s} = w_{1,|k-k_s|+1}, \tag{26}$$

One can remark clearly from (25) that the quadrature terms involving 5 points (i.e., $S_{k_s}(3)$ and $S_{k_s}(M-2)$) were scaled by $1/2$ from the original equation [23, Eq. (25.4.14)], while the remaining terms involving two, five and seven points were scaled by a factor of $1/6$ from [23, Eqs. (25.4.1)-(25.4.16)]. In fact, the area delimited by the function's curve and the $\phi'-$axis was divided in successive areas. Indeed, as represented in Fig. 3, the area $\mathcal{A}_l$ delimited by the interval $\left[\phi'_{k_s} + lh_{k_s}, \phi'_{k_s} + (l+1)h_{k_s}\right]$, $5 \le l \le M-6$ will be recomputed in the case of 7-points' interpolation by three terms on the left, i.e., $S_{k_s}(l-1)$, $S_{k_s}(l)$ and $S_{k_s}(l+1)$ as well as by three terms on the right namely, $S_{k_s}(l+2)$, $S_{k_s}(l+3)$, and $S_{k_s}(l+4)$. Therefore, each of these terms is scaled by the same factor $1/6$ to get the exact area rate. Explicitly, we have

$$\mathcal{A}_l = \sum_{i=0}^{5} S_{k_s}(l-1+i) \quad , 5 \le l \le M-6. \tag{27}$$

Besides, it can be noticed that the areas $\left[\phi'_{k_s}, \phi'_{k_s} + h_{k_s}\right]$ and $\left[\phi'_{k_s} + h_{k_s}, \phi'_{k_s} + 2h_{k_s}\right]$ are filled through the terms

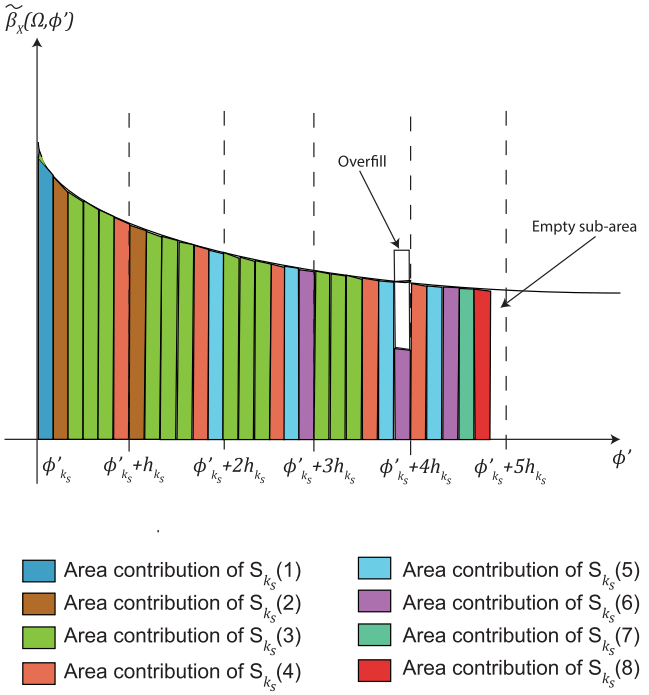

FIGURE 3. Areas rates for the adopted quadrature scheme, using the computation on 2, 3, 5, and 7 points calculated at terms $S_{k_s}(l)$; $l = 1, \ldots, M$.

$\left(S_{k_s}(1), S_{k_s}(2), S_{k_s}(3), S_{k_s}(4)\right)$ and $\left(S_{k_s}(2), S_{k_s}(3), S_{k_s}(4), S_{k_s}(5)\right)$, with scale factors $\left(\frac{1}{6}, \frac{1}{6}, \frac{1}{2}, \frac{1}{6}\right)$ and $\left(\frac{1}{6}, \frac{1}{2}, \frac{1}{6}, \frac{1}{6}\right)$, respectively. Nevertheless, there is an overfill by $\frac{1}{6}$ of the area associated to the interval $\left[\phi'_{k_s} + lh_{k_s}, \phi'_{k_s} + (l+1)h_{k_s}\right]$, for $l = 3, M-5$, as indicated in the rectangle labeled "overfill" within the interval $\left[\phi'_{k_s} + 3h_{k_s}, \phi'_{k_s} + 4h_{k_s}\right]$ in Fig. 3, as well as $\frac{1}{6}$ of the area $\left[\phi'_{k_s} + lh_{k_s}, \phi'_{k_s} + (l+1)h_{k_s}\right]$, for $l = 4$, $M-6$, not filled as represented by the blank bar within the interval $\left[\phi'_{k_s} + 4h_{k_s}, \phi'_{k_s} + 5h_{k_s}\right]$ in the same figure, within the whole area $\left[\phi'_{k_s}, \phi'_{k_s+1}\right]$. Interestingly, the 5-points scheme developed in [16] and presented in Fig. 4 is based on computing the areas $\left[\phi'_{k_s} + lh_{k_s}, \phi'_{k_s} + (l+1)h_{k_s}\right]$ ($l = 1, \ldots, M-2$) using the 2, 3, and 5-points computation, with corresponding scales of $\frac{1}{4}$, $\frac{1}{2}$, and $\frac{1}{4}$, respectively, so as to fill the whole area delimited by the ϕ' axis and the function's curve.

Remark 2: It is worthy to mention that this quadrature scheme was applied up only to 5-points quadrature scheme equivalently in [16] as depicted in Fig. 4, by considering $\left[\phi'_1, \phi'_K\right]$ as the surface of interest, and the points ϕ'_{k_s} ($1 \le k_s \le K$) as the integration points. However, this quadrature method is inaccurate considering this scheme, since the non-uniform discretization step $\Delta\phi'_{k_s}$ of each interval is relatively great (e.g., $\Delta\phi'_1 = 6°$), and consequently, that applied method is not valid.

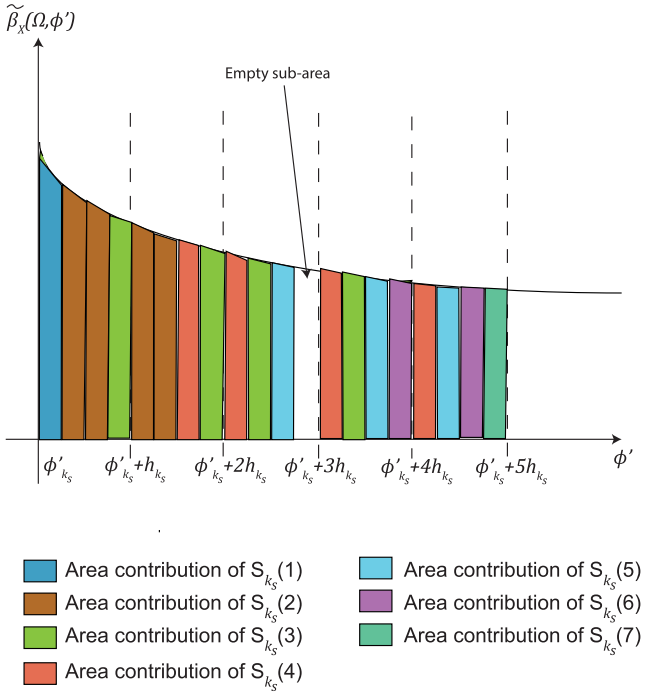

FIGURE 4. Areas rates for the 5-points quadrature scheme used in [16], using the computation on 2, 3, and 5 points calculated at terms $S_{k_s}(l)$; $l = 1, \ldots, M$.

F. FINITE DIFFERENCE EQUATION

As a third step of the process, and in order to solve the spatial derivative terms in (23), the upwind finite difference equation is involved.

The area between the transmitter and the receiver is divided into I grid points horizontally and J grid points vertically. It is noteworthy that in order to improve the computation accuracy of the upwind finite difference scheme used in [14], we involve one more point in each formula.

The Taylor-series development of the radiance function $L_{i,j,k}(t_n)$ near the four neighbor points $(i\pm1, j)$, $(i\pm2, j)$ close to (i, j), with $i = 1, \ldots, I$ and $j = 1, \ldots, J$, is given by

$$L_{i\pm1,j,k}(t_n) \approx L_{i,j,k}(t_n) \pm \Delta y \frac{\partial L_{i,j,k}(t_n)}{\partial y}, \tag{28}$$

$$L_{i\pm2,j,k}(t_n) \approx L_{i,j,k}(t_n) \pm 2\Delta y \frac{\partial L_{i,j,k}(t_n)}{\partial y}. \tag{29}$$

In a similar manner, the same development is performed at the points $(i, j \pm 1)$, $(i, j \pm 2)$.

By performing some algebraic manipulation on the equations above, and using the same reasoning likewise for the other cases of ξ_k, η_k, improved finite difference formulas are obtained as

$$\frac{\partial L_{i,j,k}(t_n)}{\partial y} \approx \begin{cases} \dfrac{2L_{i,j,k}(t_n) - L_{i-1,j,k}(t_n) - L_{i-2,j,k}(t_n)}{3\Delta y}, & \eta_k > 0 \\ \dfrac{L_{i+1,j,k}(t_n) + L_{i+2,j,k}(t_n) - 2L_{i,j,k}(t_n)}{3\Delta y}, & \eta_k < 0 \end{cases} \tag{30}$$

$$\frac{\partial L_{i,j,k}(t_n)}{\partial x} \approx \begin{cases} \dfrac{2L_{i,j,k}(t_n) - L_{i,j-1,k}(t_n) - L_{i,j-2,k}(t_n)}{3\Delta x}, & \xi_k > 0 \\ \dfrac{L_{i,j+1,k}(t_n) + L_{i,j+2,k}(t_n) - 2L_{i,j,k}(t_n)}{3\Delta x}, & \xi_k < 0 \end{cases}, \tag{31}$$

where Δx and Δy stand for the discretization steps in the x and y axes, respectively.

$$S_{k_s}(l) = \begin{cases} \dfrac{h_{k_s}}{18}\left(\widetilde{\beta}_X\left(\Omega,\phi'_{k_s}\right) + 2\widetilde{\beta}_X\left(\Omega,\phi'_{k_s}+h_{k_s}\right)\right), & l = 1, \\ \dfrac{2h_{k_s}}{36}\left(\widetilde{\beta}_X\left(\Omega,\phi'_{k_s}\right) + 4\widetilde{\beta}_X\left(\Omega,\phi'_{k_s}+h_{k_s}\right) + \widetilde{\beta}_X\left(\Omega,\phi'_{k_s}+2h_{k_s}\right)\right), & l = 2 \\ \dfrac{4h_{k_s}}{180}\left(\begin{array}{l} 7\widetilde{\beta}_X\left(\Omega,\phi'_{k_s}\right) + 32\widetilde{\beta}_X\left(\Omega,\phi'_{k_s}+h_{k_s}\right) + 12\widetilde{\beta}_X\left(\Omega,\phi'_{k_s}+2h_{k_s}\right) \\ +32\widetilde{\beta}_X\left(\Omega,\phi'_{k_s}+3h_{k_s}\right) + 7\widetilde{\beta}_X\left(\Omega,\phi'_{k_s}+4h_{k_s}\right) \end{array}\right), & l = 3 \\ \dfrac{6h_{k_s}}{5040}\left(\begin{array}{l} 41\widetilde{\beta}_X\left(\Omega,\phi'_{k_s}+(l-4)h_{k_s}\right) + 216\widetilde{\beta}_X\left(\Omega,\phi'_{k_s}+(l-3)h_{k_s}\right) + 27\widetilde{\beta}_X\left(\Omega,\phi'_{k_s}+(l-2)h_{k_s}\right) \\ +272\widetilde{\beta}_X\left(\Omega,\phi'_{k_s}+(l-1)h_{k_s}\right) + 27\widetilde{\beta}_X\left(\Omega,\phi'_{k_s}+lh_{k_s}\right) + 216\widetilde{\beta}_X\left(\Omega,\phi'_{k_s}+(l+1)h_{k_s}\right) \\ +41\widetilde{\beta}_X\left(\Omega,\phi'_{k_s}+(l+2)h_{k_s}\right) \end{array}\right); & 4 \le l \le M-3 \\ \dfrac{4h_{k_s}}{180}\left(\begin{array}{l} 7\widetilde{\beta}\left(\Omega,\phi'_{k_s+1}-4h_{k_s}\right) + 32\widetilde{\beta}\left(\Omega,\phi'_{k_s+1}-3h_{k_s}\right) + 12\widetilde{\beta}\left(\Omega,\phi'_{k_s+1}-2h_{k_s}\right) \\ +32\widetilde{\beta}\left(\Omega,\phi'_{k_s+1}-h_{k_s}\right) + 7\widetilde{\beta}\left(\Omega,\phi'_{k_s+1}\right) \end{array}\right), & l = M-2 \\ \dfrac{2h_{k_s}}{36}\left(\widetilde{\beta}_X\left(\Omega,\phi'_{k_s+1}-2h_{k_s}\right) + 4\widetilde{\beta}_X\left(\Omega,\phi'_{k_s+1}-h_{k_s}\right) + \widetilde{\beta}_X\left(\Omega,\phi'_{k_s+1}\right)\right), & l = M-1 \\ \frac{h_{k_s}}{18}\left(\widetilde{\beta}_X\left(\Omega,\phi'_{k_s+1}-h_{k_s}\right) + 2\widetilde{\beta}_X\left(\Omega,\phi'_{k_s+1}\right)\right), & l = M. \end{cases} \tag{25}$$

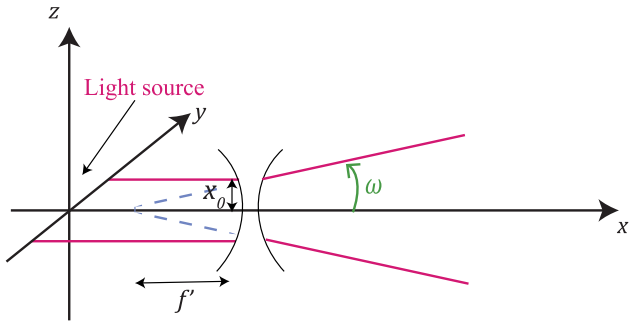

FIGURE 5. Collimated beam divergence through a divergent lens.

One can ascertain that each partial derivative is associated with two formulas depending on the sign of ξ_k and η_k.

Regarding the time derivative, the forward Euler difference formula was used as [14]

$$\frac{\partial L_{i,j,k}(t_n)}{\partial t} = \frac{L_{i,j,k}(t_{n+1}) - L_{i,j,k}(t_n)}{\Delta t}; \quad n = 1, \ldots, N-1, \tag{32}$$

with Δt being the discretization step for the time coordinate.

By plugging the partial derivatives (30), (31), and (32) into (23), and performing some manipulations, we obtain the recursive equation (33), as shown at the bottom of this page.

It is noteworthy that the above equation depicts the recursive numerical solution of the proposed TD-RTE solver for the instantaneous light radiance, in terms of the system and channel parameters, namely the source radiance, the discretization steps in space and time coordinates, the number of directions, scattering and absorption coefficient, and light celerity in the medium as well.

Without loss of generality, we consider a point source with constant power over time S_0, defined at a specific point in the transmitter plane, $\left(\text{i.e., } 1, \frac{I-1}{2}+1\right)$. In practice, the total transmit power is radiated in the form of a collimated beam, through a divergent optical lens with a certain focal length f' with an associated divergence half-angle ω, so as to produce a divergent beam [11]. f' and ω are related as

$$f' = -\frac{x_0}{\omega}, \tag{34}$$

with x_0 being the beam waist radius at the lens as shown in Fig. 5. In this case, the source radiance equals to the ratio between the source power and a circular surface of radius x_0 and to the divergence angle 2ω.

Remark 3: It is worthy to mention that by neglecting the radiance variations over time $\left(\text{i.e., } \frac{\partial L_{i,j,k}(t)}{\partial t} = 0\right)$, *the light radiance* $L_{i,j,k}(t_n)$ *becomes time-independent. That is, the TD-RTE equation in (33) becomes TI-RTE expressed as*

$$L_{i,j,k}^{(l+1)} = \left(\frac{1}{\mp\frac{2\eta_k}{3\Delta y} \mp \frac{2\xi_k}{3\Delta x} + c}\right)\left(\mp\eta_k \frac{L_{i\pm1,j,k}^{(l)} + L_{i\pm2,j,k}^{(l)}}{3\Delta y} \mp\xi_k \frac{L_{i,j\pm1,k}^{(l)} + L_{i,j\pm2,k}^{(l)}}{3\Delta x} + b\sum_{k_s=1}^{K} w_{k,k_s} L_{i,j,k_s}^{(l)} + S_0\right), \tag{35}$$

where l denotes the solution iteration index.

G. RECEIVED POWER CALCULATION

In our analysis, the receiver is placed on the *YOZ* plane. Knowing that the calculated radiance is performed in the *XOY* plane, the received power is calculated by summing up the light radiance at grid points in the receiver plane perpendicular to the $x-$axis (i.e., *YOZ* plane). Without loss of generality, we assume that the receiver aperture placed at the receiver plane is divided into $\frac{\Delta y}{2}-$equidistant circular surfaces, being defined as [10]

$$A_l = \begin{cases} \pi\left(\frac{\Delta y}{2}\right)^2, & l = 1 \\ 2\pi\,(\Delta y)^2\,(l-1), & 2 \le l \le L \end{cases}, \tag{36}$$

where L denotes the number of the circular surfaces within the receiver aperture given in terms of the receiver aperture of radius R

$$L = \frac{R}{\Delta y}. \tag{37}$$

Let $\Delta\phi'_p$, with $1 \le p \le P$, denotes the difference between two directions ϕ'_p and ϕ'_{p+1} within the receiver FOV in the *XOY* plane, discretized in the same way as the scattering angles following equation (21) and (22), with P denotes the total number of discrete directions within the receiver FOV. Without loss of generality, the radiance within the angle interval delimited by $\Delta\phi'_p$ in *XOY* plane, is assumed to be constant. By considering also symmetric scattering in the elevation direction, the surface power density is uniform within each elementary circular surface within the receiver aperture. Therefore, the total received power can be expressed as [10]

$$P_r(t_n) = \sum_{l=1}^{L} A_l \sum_{p=1}^{P} \Delta\phi'_p L_{l+\left(\frac{l-1}{2}\right),J,p}(t_n), \; n = 1, \ldots, N, \tag{38}$$

Thus, Algorithm 2 depicts the power computation process. As an initial step, *optimal non-uniform scattering angles*

$$L_{i,j,k}(t_{n+1}) = L_{i,j,k}(t_n)\left[1 - cv\Delta t \pm \frac{2\eta_k v\Delta t}{3\Delta y} \pm \frac{2\xi_k v\Delta t}{3\Delta x}\right] \mp \eta_k v\Delta t \frac{L_{i\pm1,j,k}(t_n) + L_{i\pm2,j,k}(t_n)}{3\Delta y} \mp\xi_k v\Delta t \frac{L_{i,j\pm1,k}(t_n) + L_{i,j\pm2,k}(t_n)}{3\Delta x} + bv\Delta t \sum_{k_s=1}^{K} w_{k,k_s} L_{i,j,k_s}(t_n) + v\Delta t S_0. \tag{33}$$

Algorithm 2 RTE Power Computation

Data: K, g, α, g_1, g_2, μ, n_p, ϵ, SPF, Δx, Δy, Δt, t_N, x_{max}, y_{max}, R, S_0, FOV, P
Result: $L_{i,j,k}(t_n)$,$P_r(t_n)$
begin
- Discretize ϕ'_k with non-uniform distribution ϕ'_k= **Optimal scattering angles** $\left(K, g, \alpha, g_1, g_2, \mu, n_p, \epsilon, SPF\right)$, $1 \leq k \leq K$;
- Computing the quadrature terms w_{k,k_s} for $k, k_s \in [1, K]$ using (25) and (26);
- $I \leftarrow \lfloor \frac{y_{max}}{\Delta y} \rfloor + 1$;
- $J \leftarrow \lfloor \frac{x_{max}}{\Delta x} \rfloor + 1$;
- $\phi'_p \leftarrow \phi'_k$ for $\phi'_k \in FOV$, $k = 1, \ldots, K, p = 1, \ldots, P$;
- $L \leftarrow \frac{R}{\Delta y}$;
- $N \leftarrow \lfloor \frac{t_N}{\Delta_t} \rfloor + 1$;
- Calculate iteratively the radiance $L_{i,j,k}(t_n)$ using (33) for $i = 1, \ldots, I, j = 1, \ldots, J$, $k = 1, \ldots, K$, and $n = 1, \ldots, N$;
- Evaluate the total received power $P_r(t_n)$, using (38) ;

end

discretization is performed using Algorithm 1, where these angles will be used to compute the quadrature terms w_{k,k_s} so as to evaluate the integral term in (6), using (25) and (26). Afterwards, a uniform space discretization on the x and y axes as well as time discretization are performed, based on which the radiance $L_{i,j,k}\ (t_n)$ at a given point, time instant and direction is computed. At the receiver side, given a discretized aperture surface and a receiver FOV, the collected power is computed at the receiver aperture, as a function of time, based on the evaluated radiance in the receiver plane.

It is worthy to mention that the Matlab code of Algorithm 2 for the RTE resolution and power computation is presented in Appendix, as well as in [18].

III. BER PERFORMANCE OF UOWC

In this section, and based on the derived results, we investigate the bit error rate (BER) performance of the underwater optical wireless communication system subject to absorption and scattering, in terms of channel and system parameters.

A. SIGNAL-TO-NOISE RATIO

The instantaneous signal-to-noise ratio (SNR) at the output of a receiver employing the direct detection technique, in the presence of thermal and shot noise, is expressed as [7], [16], [24]

$$SNR\left(t_n\right) = \frac{I_P^2(t_n)}{N_0} = \frac{\left(R_s F P_r\left(t_n\right)\right)^2}{\sigma_s^2 + \sigma_{th}^2}, \qquad (39)$$
$$= \frac{\left(R_s F P_r\left(t_n\right)\right)^2}{2q(I_P(t_n) + I_D)B_w + \frac{4\kappa T_e B_w}{R_L}},$$

where

- $I_P(t_n)$: Incident light photo current (A),
- N_0 : Total noise power (W),
- R_s : Photodetector responsivity (A/W),
- F : Photodetector gain factor ($F = 1$ for PIN photodetector),
- σ_s^2 : Shot noise power (W),
- σ_{th}^2 : Thermal noise power (W),
- q : Electrical elementary charge $(1.6 \times 10^{-19} C)$,
- I_D : Shot noise dark current (A),
- B_w : Electrical filter bandwidth (Hz),
- κ : Boltzmann constant $(J \cdot K^{-1})$,
- T_e : Receiver temperature (K),
- R_L : Electrical receiver load resistance (Ω).

B. BIT ERROR RATE

The BER of a communication system employing On-Off Keying (OOK) modulation scheme, with respect to a received SNR is defined as [7, Eq. (4.24)]

$$P_e\left(t_n\right) = Q\left(\sqrt{SNR(t_n)}\right)$$
$$= Q\left(\frac{R_s F P_r\left(t_n\right)}{\sqrt{2q(I_P(t_n) + I_D)B_w + \frac{4\kappa T_e B_w}{R_L}}}\right), \qquad (40)$$

with $Q\left(\cdot\right)$ denotes the Gaussian Q-function [25, Eq. (4.1)]. Note that the values of R_s, F, and I_D can be usually retrieved from the datasheet of the photodiode product.

IV. PERFORMANCE AND COMPLEXITY EVALUATIONS

This section presents the evaluation performance of the proposed TD-RTE solver in terms of computation accuracy as well as complexity. The TD-RTE results are given in three dimensions (3D) as a function of the propagation distance as well as time instants, while the TI-RTE results are shown in two dimensions (2D) versus the distance. The respective MATLAB codes of the proposed RTE solver are available in [18]. The RTE and MC simulations complexities are depicted in terms of time consumption per each computation step. We depict a single scattering scenario per each SPF among the three considered phase functions, for fixed values of $g = 0.93$ for the STHG function, $\alpha = 0.9832, g_1 = 0.8838, g_2 = -0.9835$ for the TTHG function, while we set $n = 1.33$, $\mu = 3.483$ for the Fournier-Forand scattering model. Two water types are taken into account, namely Harbor-I ($b = 0.91$, $c = 1.1$) and Harbor-II ($b = 1.8177$, and $c = 2.2$) waters with: $Y = 20$ cm as the tank altitude, $t_N = 20$ ns, $\Delta x = 5$ cm, $\Delta y = 1$ cm, and $\Delta t = 25$ ps as the discretization steps in the x-axis, y -axis, and time coordinate, respectively, and $K = 22$ as the number of discrete directions. Additionally, we considered a transmitting optical lens with a beam waist radius of $x_0 = 1$ mm. The values of R_s, I_D, and T_e were taken from [24]. The respective Monte Carlo results were performed based on the simulations provided in [11]. In this regard, the CDF numerical computation in this last-mentioned was modified in order to evaluate the CDF

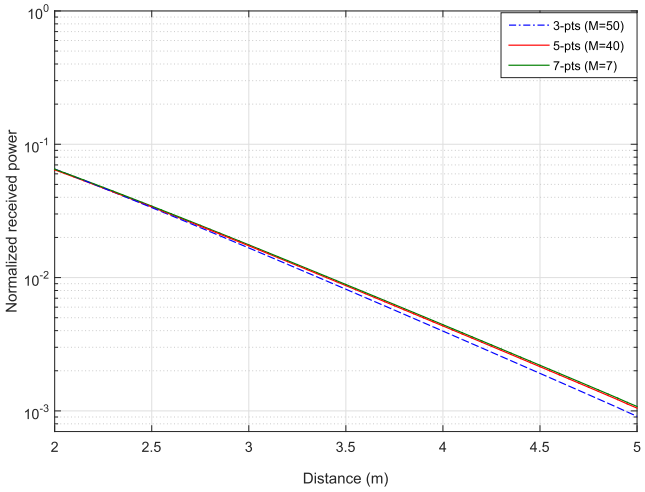

FIGURE 6. Normalized received power versus propagation distance in a Harbor-II turbid water medium for the STHG function.

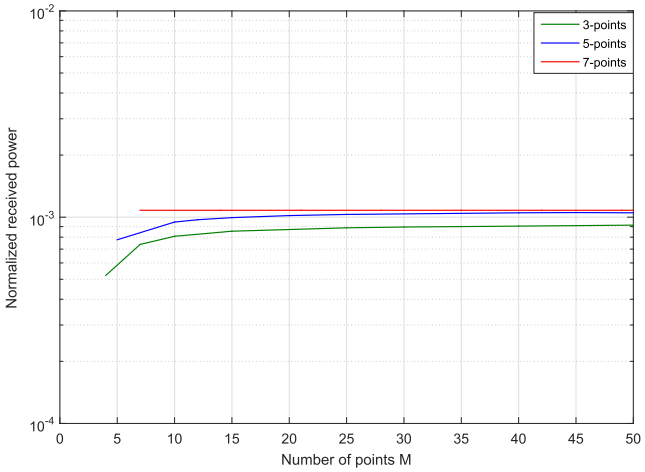

FIGURE 7. Normalized received power versus M for Harbor-I.

with respect to the generated scattering angles accurately. Furthermore, the number of generated angles was adjusted as a function of the propagation distance.

Figs. 6 and 7 depict the TI-RTE normalized received power results over time versus the distance and the number of points M, over Harbor-II and Harbor-I, respectively, assuming STHG SPF. Actually, determining the number of discrete points M within each interval $[\phi'_{k_s}, \phi'_{k_s+1}]$ is of paramount importance to improve the accuracy of the proposed RTE solver. Particularly, we depict the RTE solver behavior using the considered quadrature schemes, namely 3-points, 5-points, and 7-points schemes. One can remark clearly that the curves corresponding to 3-points and 5-points schemes converge to the exact solution by increasing the number of discretization points M (lower discretizing step h_{k_s}) within each surface $[\phi'_{k_s}, \phi'_{k_s+1}]$ (i.e., $M = 50$ for 3-points, and $M = 40$ for 5-points), while for the 7-points scheme, the convergence needs a lesser number of points than for the 3-points and 5-points schemes (i.e., $M = 7$).

TABLE 1. Evaluation time of the numerical integration quadrature schemes (in seconds).

K \ Quadrature Scheme	3 points	5 points	7 points
22	0.0139	0.0132	0.0017
26	0.0147	0.0134	0.0027
30	0.0187	0.0148	0.0052
35	0.0175	0.0142	0.0063
40	0.0229	0.0151	0.0070
50	0.0276	0.0165	0.0078

In terms of computation complexity of the adopted quadrature schemes, Table 1 shows the evaluation time in seconds of the implemented 7-points quadrature scheme, for various values of the scattering angles number K, compared with the 3 and 5-points schemes developed in [10] and [16], respectively. These last-mentioned schemes were adapted similarly as performed to the 7-points scheme, where they were applied for infinitesimally small sub-intervals between two successive scattering angles. Additionally, the respective number of points M within each subinterval of two successive scattering angles is taken as $M = 7$, 40, and 50 for the 3, 5, and 7-points schemes, respectively. Interestingly, it can be noticed that the 7-points scheme is 8-20 ms less than its 3 and 5 counterparts. In fact, the higher the number of points M, the greater the computation time needed. Furthermore, one can ascertain that the time consumption increases slightly as a function of K for the aforementioned schemes. Additionally, it can be obviously seen that the total consumed time slightly differs between the 3 schemes. In fact, since the quadrature weight coefficients are calculated once and outside the main loops (*i.e.*, $i = 1, \ldots, I$; $j = 1 \ldots, J$; $k = 1, \ldots, K$; $n = 1, \ldots, N$), the computation time is not impacted significantly.

Figs. 8-10 depict the TD-RTE normalized received power result versus distance and time, for Harbor-I, in three dimensions, taking into account the considered SPFs (STHG, TTHG, and FF). One can ascertain that the received power decreases as a function of the distance, i.e., the farther the communication nodes are, the higher the power path-loss is due to water attenuation phenomena. Moreover, we ascertain that at initial time instants, the received power at a given distance is lower initially and starts gradually increasing as a function of time until reaching the convergence level when the received power remains constant in time. Actually, at initial time instants, few photons reach the receiver plane, and consequently, it results in lower received power. More photons reach the receiver side resulting in an increase of the received power versus time.

Figs. 11-13 depict the TI-RTE average normalized received power results over time, in two dimensions, computed by RTE numerical solver as well as the respective Monte Carlo results by considering the adopted volume scattering functions (i.e., STHG, TTHG, and FF). We can notice obviously that

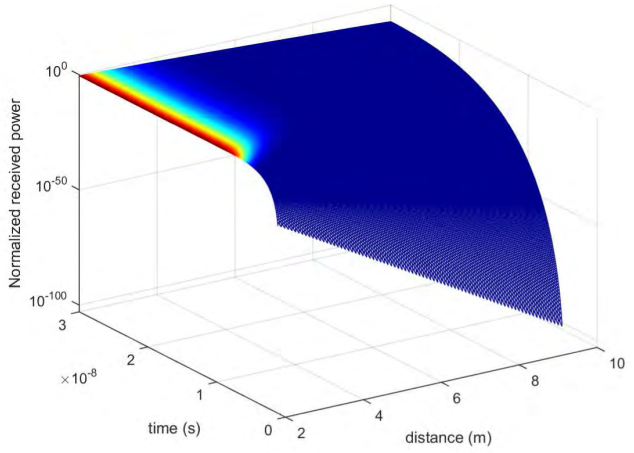

FIGURE 8. Normalized received power in 3D versus distance and time, considering STHG function and a receiver aperture of 10cm.

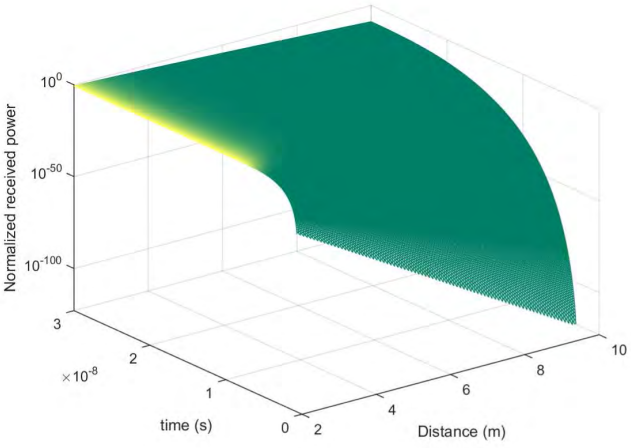

FIGURE 9. Normalized received power in 3D versus distance and time, considering TTHG function and a receiver aperture of 10cm.

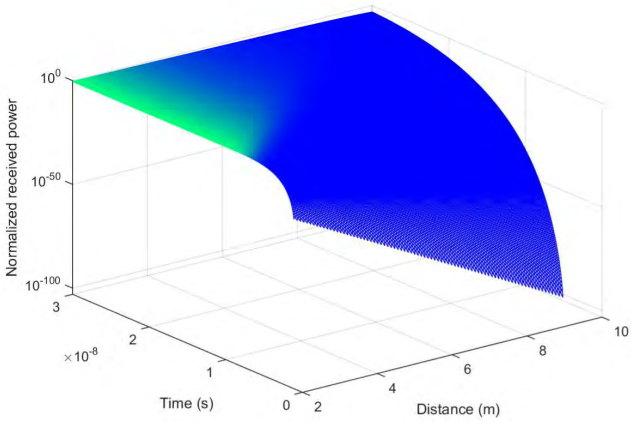

FIGURE 10. Normalized received power in 3D versus distance and time, considering FF function and a receiver aperture of 10cm.

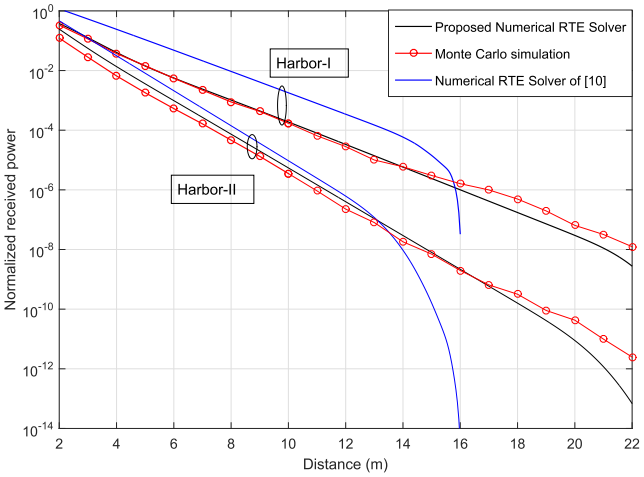

FIGURE 11. Average normalized received power over time versus distance considering STHG function and a receiver aperture 10cm.

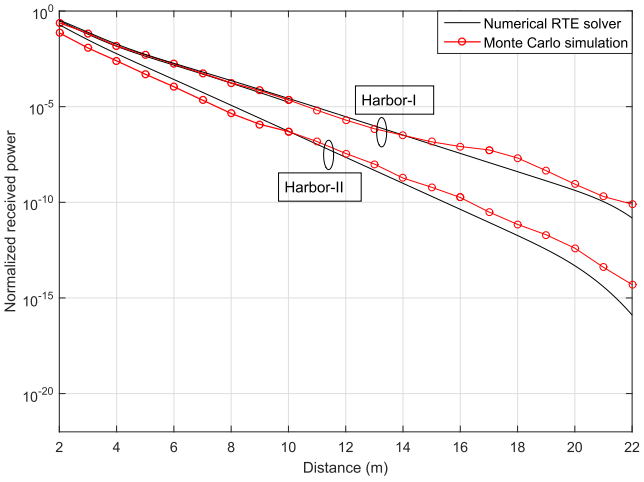

FIGURE 12. Average normalized received power over time versus distance considering TTHG function and a receiver aperture 10cm.

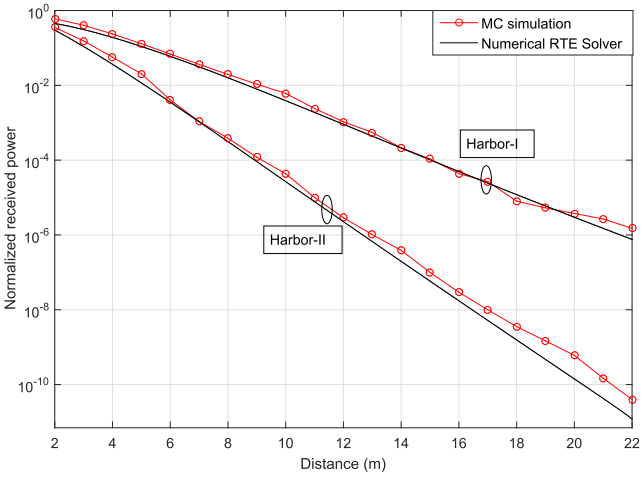

FIGURE 13. Average normalized received power over time versus distance considering FF function and a receiver aperture 10cm.

the power loss in Harbor-II water type is more significant than the Harbor-I case. That is, the higher the scattering and absorption coefficients are (i.e., ($a = 0.187$, $b = 0.913$) for Harbor-I and ($a = 0.374$, $b = 1.81$) for Harbor-II), the greater is the path-loss, and consequently, the system performance degrades. For instance, in Fig. 11, the power-loss reaches -80 dB at a distance of 15m for

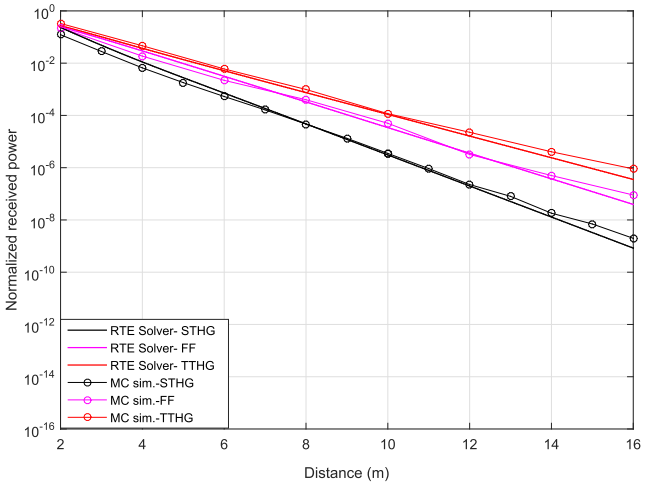

FIGURE 14. Normalized received power comparison for the three considered SPFs, over Harbor-II and $B_p = 0.0183$.

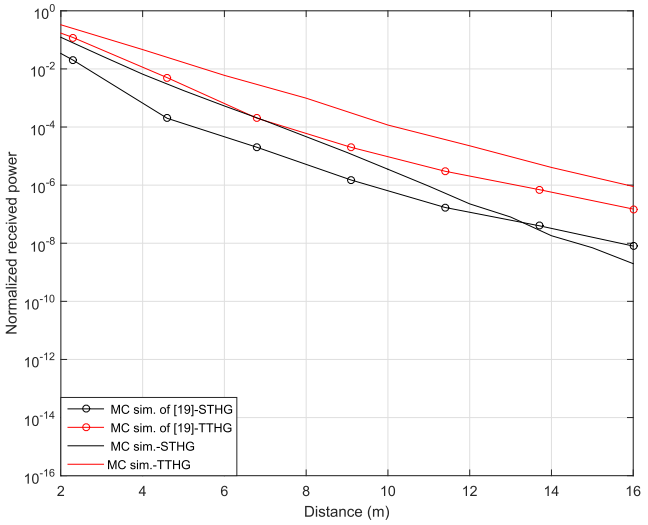

FIGURE 15. Comparison between two MC simulation methods over Harbor-II water type.

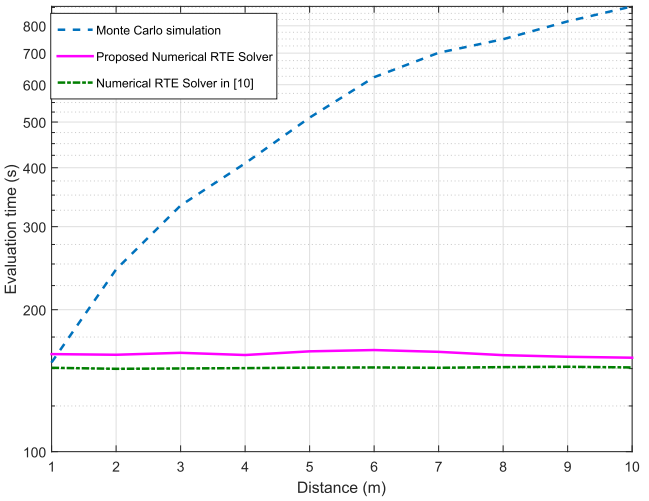

FIGURE 16. Evaluation time comparison between Numerical RTE Solver and Monte Carlo simulation.

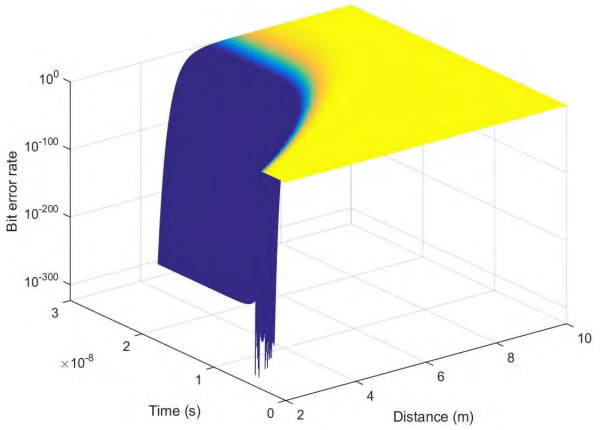

FIGURE 17. Bit error rate performance of the considered system in 3D, based on time-dependent RTE resolution considering STHG function over Harbor-I (aperture: 10cm).

Harbor-II, while it is around −55 dB for the Harbor-I case at the same distance. Additionally, for Fig. 11, one can note clearly the close matching between the proposed numerical RTE curves and results considering STHG function, more particularly in Harbor-I water type, while the accuracy for Harbor-II is tight up to a distance 19m, which above it a gap is noticed. On the other hand, the RTE solver proposed in [10] diverges from MC curves, particularly at higher distances for both considered water types, which proves the accuracy of the proposed numerical solver. In a similar manner to the STHG case in Fig. 11, the path-loss in Figs. 12-13 for Harbor-II medium is more significant than its Harbor-I counterpart. Additionally, MC simulation results show a good agreement with the RTE numerical ones in Fig. 12 for the TTHG case, while a slight difference is noticed again at higher distances for both cases. Importantly, one can notice in Fig. 13 the accuracy of the proposed RTE solver over the FF SPF for Harbor-I case.

Fig. 14 presents a comparative plot of the three considered SPFs over Harbor-II water type, where their respective parameters were chosen from [19] and [20], such as to have the same backscattering ratio $B_p = 0.0183$ (i.e., $g = 0.9185$, $\alpha = 0.9843$, $g_1 = 0.9809$, $g_2 = 0.6922$, $\mu = 3.5835$, $n_p = 1.10$). It has been shown in [20] that this configuration of parameters yields the best approximation with Petzold's measured SPF over turbid Harbor waters. MC simulations, performed with the same abovementioned set of parameters, are presented also. We can notice in this figure the effect of the adopted SPF on the normalized power. Actually, under the same backscattering ratio value, all the considered SPFs yield close results to their MC counterparts. Additionally, we can notice also that the STHG SPF model least power value.

In Fig. 15, another comparative plot of the STHG and TTHG phase functions is shown, evaluated over Harbor-II water type through the adopted MC simulations, and the ones provided in [19]. The scattering strength g was set as

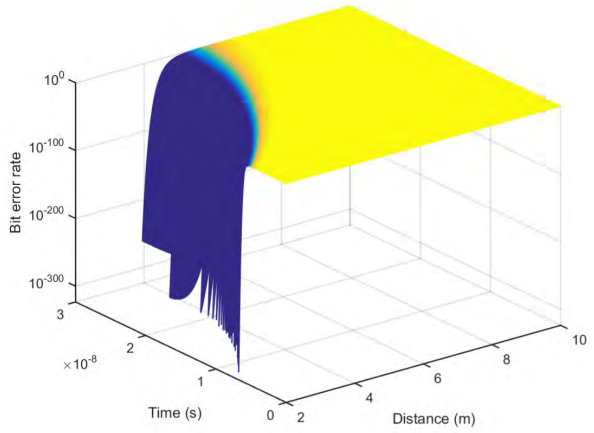

FIGURE 18. Bit error rate performance of the considered system in 3D, based on time-dependent RTE resolution considering TTHG function over Harbor-I (aperture: 10cm).

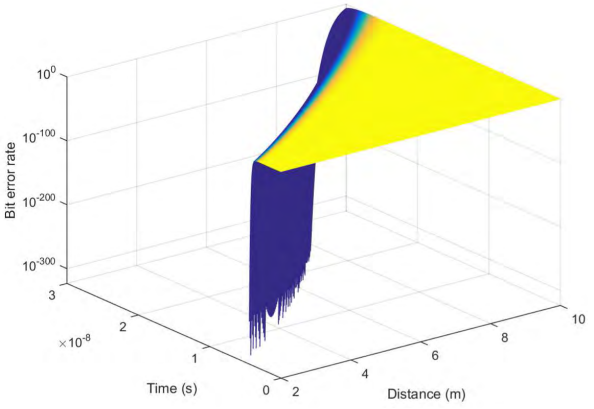

FIGURE 19. Bit error rate performance of the considered system in 3D, based on time-dependent RTE resolution considering FF function over Harbor-I(aperture: 10cm).

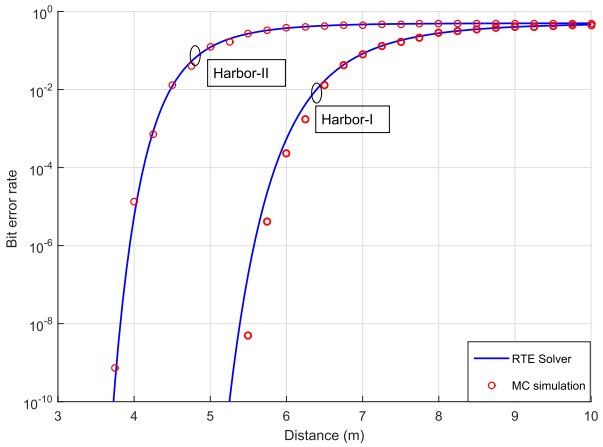

FIGURE 20. Bit error rate performance of the considered system based on the average received power over time, considering STHG function (aperture: 10cm).

$g = 0.924$ of the STHG as chosen in [19], and $\alpha = 0.9854$, $g_1 = 0.9823$, $g_2 = 0.6937$ for the TTHG SPF, so as to produce a value of $B_p = 0.0170$. We can notice that the adopted

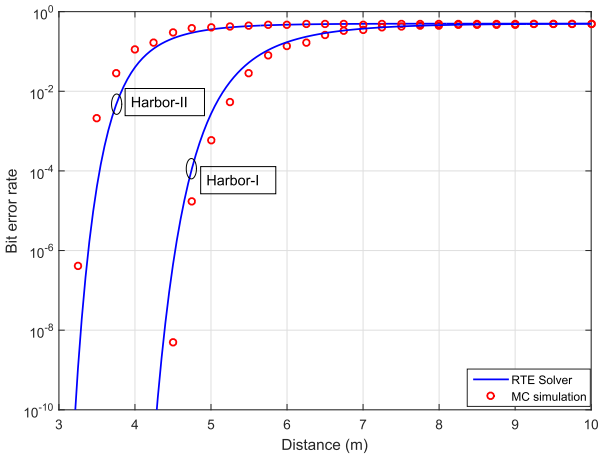

FIGURE 21. Bit error rate performance of the considered system based on the average received power over time, considering TTHG function (aperture: 10cm).

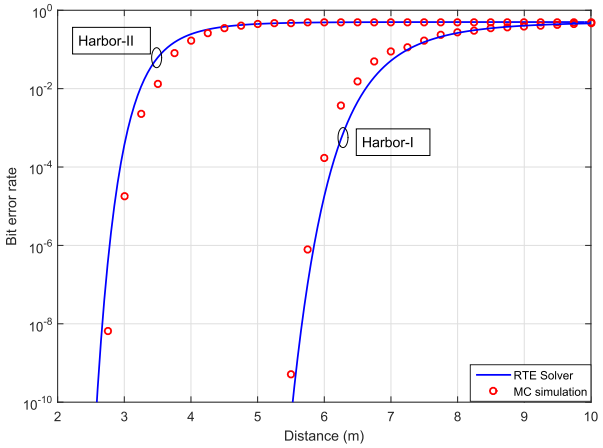

FIGURE 22. Bit error rate performance of the considered system based on the average received power over time, considering FF function (aperture: 10cm).

MC simulation yields a less path-loss compared to the MC simulation results of [19], for the STHG case, while this last-mentioned exceeds the adopted MC simulation for distances beyond 13 m. In contrast, for the TTHG SPF, the adopted MC simulation result exhibits a lesser power-loss over the whole distance range below 16 m. This difference is due to the fact that the adopted MC simulation was performed by optimizing throughout the propagation distances the number of discretized scattering angles.

Fig. 16 depicts the total time consumption comparison between the proposed numerical RTE solver and Monte Carlo simulation, computed for Harbor-I water type. One can notice clearly the logarithmic increase of the MC scheme time consumption in the log-scale, which corresponds to a linear increase in the linear scale. On the other hand, we remark also that the computation time of the proposed RTE solver as well as the one proposed in [10] remain constant. In addition to this, we can notice that the respective complexities of the

proposed RTE solver and the one in [10] are very close, in terms of computation complexity. Importantly, the main outcome of this result is the difference in complexity between the proposed numerical RTE solver and its MC counterpart. That is, the numerical RTE solver can achieve accurate results, with a remarkably reduced complexity compared to MC method.

Figs. 17-22 depicts the BER performance of the communication system in 2D and 3D, based on (40) for both water types, for the considered VSF functions. The 2D curves correspond to the average normalized received power over time. In a similar manner to the power behavior, one can remark obviously that the BER increases as a function of the propagation distance. That is, the greater the propagation distance is, the more important is the path-loss, and consequently, the BER performance degrades. Additionally, the BER decreases with the increase of the received power as a function of the time. Also, Harbor-I water type exhibits a lower bit error rate to Harbor-II one.

V. CONCLUSION

In this paper, an improved time-dependent RTE numerical evaluation algorithm is proposed, in order to solve the radiative transfer equation that quantifies the light propagation loss in the underwater medium. The proposed RTE solver was applied for three types of scattering phase functions namely, the STHG, TTHG, and FF SPFs. Boole's rule given by the 5-points and 7-points Newton-Cotes formula was incorporated as a quadrature method alongside with the two and three points Simpson's method in order to solve the integral term. The upwind finite difference scheme was also improved by adding one more neighbor point. Furthermore, the MSE-based algorithm for scattering angles discretization was modified from [10], [16]. The received light power was calculated in terms of system and channel parameters, such as propagation distance, time, absorption and scattering coefficient, as well as the number of angles. Based on this result, the BER performance of the considered UOWC system was analyzed in terms of the system and channel parameters. The proposed RTE numerical solver and Monte Carlo simulations have been compared in terms of tightness and complexity, where the results present a good agreement between RTE and MC results. Furthermore, the results show that the proposed solver has significantly less complexity compared to its MC counterpart. Matlab codes of the proposed RTE solver have been presented. From another perspective, we can conclude also by these results that the path-loss in underwater communication systems is significantly high, where the power-loss can reach around -55 dB for Harbor-I and -80 dB for Harbor-II water type, at a distance of 15 m, as depicted in Fig. 11. Consequently, the respective BER is very high. To this end, several solutions and recommendations can be advocated in

```
 % %   Main   code   for   the   RTE   Solver
 function y=RTE_solver(c,albedo,start,length_y,length_z,
     step_y,step_z,aperture,K,g,alph,g1,g2,mu,nn,ord,SPF)
b=c*albedo;
I=(length_y/step_y)+1;
M= floor(aperture/step_y)+1;
r(1)=step_y/2;
s= zeros(1,(M-1)/2+1);
s(1,1)= pi*r(1)^2;
 for n=2:(M-1)/2+1
r(n)=r(n-1)+step_y;
s(n)= pi*r(n)^2-s(n-1);
 end
    J=(length_z/step_z)+1;
    q= zeros(I,J,K);
q(((I-1)/2)+1,1,1)=1;  % %   source   at   the   middle
 % %   Non - Uniform   discretization
phi=rte_angle_dist_org_pr_biss(g,alph,g1,g2,mu,nn,1+K/2,
     SPF);
 % %   Computing   weight   coefficients   of   the
     integral   term
 [tt,w, theta]=weight_biss_pr(phi,K,g,alph,g1,g2,mu,nn,
     ord,SPF);
   % %   iterative   computing   of   the   received
      radiance
 [radiance]=gauss_rte_biss_p(w,theta,length_y,length_z,
     step_y,step_z,K,q,b,c);
 intensity= zeros(I,J);
  phi(K+1)=2* pi+0.0015/2;
    for k=1:K
 % %   Field   of   view   test
 if ((phi(k)>=0 && phi(k)<= pi))
intensity(:,:)=intensity(:,:)+radiance(:,:,k)*(phi(k+1)-
     phi(k));
 end
    end
 % %   power   computation
 for jj=1:J
powerr(jj)=s*intensity((I-1)/2+1:(M-1)/2+(I-1)/2+1,jj);
 end
 for ii=1:1:J-start/step_z
powertrc(ii)=powerr(ii+start/step_z);
 end
 tm= toc
z=start:step_z:length_z;
 semilogy(z,powertrc_7./( pi*10^-6),'r-.')
 grid on;
```

```
 % %   Non - uniform   angles   discretization
 function y=rte_angle_dist_org_pr_biss(g,alph,g1,g2,mu,nn
     ,N,SPF)
 % %   1- initializing   directions   uniformly
maxit=550;  %   max   number   of   iterations :   MSE
     convergence   criterion
 if ( strcmp(SPF,'STHG')==1)
 % %%   STHG   function

bta1=@(teta) teta.*(1-g.^2)./(2.* pi.*(1+g.^2-2.*g.*
     cos(teta)));

bta2=@(teta) (1-g.^2)./(2.* pi.*(1+g.^2-2.*g.*
     cos(teta)));
 elseif ( strcmp(SPF,'TTHG')==1)
 % %   3 D
 %   %%   TTHG   function
bta1=@(teta) teta.*(alph*(1-g1.^2)./(2.*
     pi.*(1+g1.^2-2.*g1.*
     cos(teta)))+(1-alph)*(1-g2.^2)./(2.*
     pi.*(1+g2.^2-2.*g2.* cos(teta))));

bta2=@(teta) alph*(1-g1.^2)./(2.* pi.*(1+g1.^2-2.*g1.*
     cos(teta)))+(1-alph)*(1-g2.^2)./(2.*
     pi.*(1+g2.^2-2.*g2.* cos(teta)));
 %     %%   Fournier - Forand   function
 elseif ( strcmp(SPF,'FF')==1)
 v=(3-mu)/2;
dlt=@(teta) 4/(3*(nn-1)^2).*( sin(teta/2)).^2;
dlt_pi=4/(3*(nn-1)^2);
 bta1=@(teta) teta.* 1./(4* pi*(1-dlt(teta)).^2.*dlt(teta
     ).^v).*(v.*(1-dlt(teta))-(1-dlt(teta).^v)+(dlt(teta)
     .*(1-dlt(teta).^v)-v.*(1-dlt(teta))).*(
     sin(teta./2)).^(-2))+...
     (1-dlt_pi^v)./(16* pi*(dlt_pi-1).*dlt_pi^v).*(3.*(
         cos(teta)).^2-1);

 bta2=@(teta)  1./(4* pi*(1-dlt(teta)).^2.*dlt(teta).^v)
     .*(v.*(1-dlt(teta))-(1-dlt(teta).^v)+(dlt(teta).*(1-
     dlt(teta).^v)-v.*(1-dlt(teta))).*(
     sin(teta./2)).^(-2))+...
     (1-dlt_pi^v)./(16* pi*(dlt_pi-1).*dlt_pi^v).*(3.*(
         cos(teta)).^2-1);
 else
     fprintf('\n Invalid entry for the SPF\n');
```

```
  end
  % %   1-     Uniform   distribution   of   angles
 phi=rte_unif_dist_org(N);

  % %   2-   computing   t ( k )   vector   for   k =1: N
      -1
 t= zeros(1,2*(N-1)+1);
 t(1)=0.0015/2;  %   t (0) =0
 for kk=1:maxit

     for jj=1:2*(N-1)-1
   t(jj+1)=(phi(jj)+phi(jj+1))/2;
     end
    t(2*(N-1)+1)=(phi(2*(N-1))+2* pi)/2;

     for ii=1:2*(N-1)
   phi(ii)=integral (bta1,t(ii),t(ii+1))./integral(bta2,t
        (ii),t(ii+1));
     end

 end
y=phi;
 end
```

```
   % %   computes   the   weight   coefficients
      associated   to   the   quadrature   method
  function [tt,w,theta]=weight_biss_pr(x,N_angle,g,alph,
      g1,g2,mu,nn,ord,SPF)
 tic
w= zeros(N_angle,N_angle);
m=(N_angle+2)/2;
 % %%   STHG   function
 if( strcmp(SPF,'STHG'))
f=@(x) (1-g^2)./(2* pi*(1+g^2-2*g* cos(x)));  % 2 D
 elseif( strcmp(SPF,'TTHG'))
 % %%   TTHG   function
 f=@(x) alph*(1-g1^2)./(2* pi*(1+g1^2-2*g1*
      cos(x)))+(1-alph)*(1-g2^2)./(2* pi*(1+g2^2-2*g2*
      cos(x)));
 elseif( strcmp(SPF,'FF'))
 % %   Fournier   Forand   function
v=(3-mu)/2;
dlt=@(x) 4/(3*(nn-1)^2).*( sin(x/2)).^2;
dlt_pi=4/(3*(nn-1)^2);
f=@(x)   1./(4*
     pi*(1-dlt(x)).^2.*dlt(x).^v).*(v.*(1-dlt(x))-(1-dlt(x
      ).^v)+(dlt(x).*(1-dlt(x).^v)-v.*(1-dlt(x))).*(
      sin(x./2)).^(-2))+...
      (1-dlt_pi^v)./(16* pi*(dlt_pi-1).*dlt_pi^v).*(3.*(
          cos(x)).^2-1);
 else
 fprintf('\nInvalid␣entry␣for␣the␣SPF\n');
 end

 for ll=1:m-1
 %   for   ll =1: m
h1=x(ll);
h2=x(ll+1);
M=7;
h=(h2-h1)/(M-1);
     ss= zeros(1,M);
     tt= zeros(1,M);
     uu= zeros(1,M);
      if (ord==3)
 % %%%%%%%%%   3   points   scheme
       % %2   pts
     uu(1)=1/6*(2*f(h1)+f(h1+h))*h;
uu(M)=1/6*(f((M-2)*h)+2*f((M-1)*h))*h;
 % %   3   points

 %   3   points
 for ii=2:M-1
     uu(ii)=1/12*(f(h1-(ii-2)*h)+4*f(h1+(ii-1)*h)+f(h1+ii*
         h))*2*h;
 end
w(1,ll)= sum(uu);


      elseif (ord==5)
    % %%%%   5   points   scheme
    % %2   pts
tt(1)=1/12*(2*f(h1)+f(h1+h))*h;
tt(M)=1/12*(f((M-2)*h)+2*f((M-1)*h))*h;
 % %   3   points
tt(2)=1/12*(f(h1)+4*f(h1+h)+f(h1+2*h))*2*h;
tt(M-1)=1/12*(f(h2-2*h)+4*f(h2-h)+f(h2))*2*h;
% %   5   points
for ii=3:M-2
   tt(ii)=1/360*(7*f(h1+(ii-3)*h)+32*f(h1+(ii-2)*h)+12*f
        (h1+(ii-1)*h)+32*f(h1+(ii)*h)+7*f(h1+(ii+1)*h))
       *(4*h);
end
w(1,ll)= sum(tt);
```

```
      elseif (ord==7)
  %   %%%%%%   7   points   scheme

   % %2   points
ss(1)=1/18*(2*f(h1)+f(h1+h))*h;
ss(M)=1/18*(f((M-2)*h)+2*f((M-1)*h))*h;
 % %   3   points
ss(2)=1/36*(f(h1)+4*f(h1+h)+f(h1+2*h))*2*h;
ss(M-1)=1/36*(f(h2-2*h)+4*f(h2-h)+f(h2))*2*h;
 % %   5   points
ss(3)=1/90*1/2*(7*f(h1)+32*f(h1+h)+12*f(h1+2*h)+32*f(h1
     +3*h)+7*f(h1+4*h))*(4*h);
ss(M-2)=1/90*1/2*(7*f(h2-4*h)+32*f(h2-3*h)+12*f(h2-2*h)
     +32*f(h2-h)+7*f(h2))*(4*h);
 % %   7   points
 for ii=4:M-3
    ss(ii)=1/840*1/6*(41*f(h1+(ii-4)*h)+216*f(h1+(ii-3)*h
         )+27*f(h1+(ii-2)*h)+272*f(h1+(ii-1)*h)+27*f(h1+(
         ii)*h)+216*f(h1+(ii+1)*h)+41*f(h1+(ii+2)*h))*(6*h
         );
 end

w(1,ll)= sum(ss(1:M-1));

     else
         fprintf('the␣provided␣order␣number␣is␣neither␣3,
             ␣nor␣5,␣7␣!!!␣Provide␣one␣of␣those␣integers')
     end
w(1,2*m-1-ll)=w(1,ll);

 end

w(1,:)=w(1,:)/ sum(w(1,:));
 for ii=2:N_angle
 for j=1:N_angle
w(ii,j)=w(1, abs(ii-j)+1);
 end
 end

theta= zeros(N_angle,2);

 for ii=1:N_angle

theta(ii,1)= cos(x(ii));
 theta(ii,2)= sin(x(ii));
 end

tt= toc
 end
```

```
  % %   iterative   computing   of   the   received
      radiance
  function [y]=gauss_rte_biss_p(w,theta,length_y,length_z,
      step_y,step_z,K,q,b,c)
I=(length_y/step_y)+1;
J=(length_z/step_z)+1;
radiance= zeros(I,J,K);
radiance_temp= zeros(I,J,K);

 for l=1:320
 for k=1:K
denominator1(k)=2*theta(k,2)/(3*step_y)+2*theta(k,1)/(3*
      step_z)+c;
denominator2(k)=2*theta(k,2)/(3*step_y)-2*theta(k,1)/(3*
      step_z)+c;
denominator3(k)=-2*theta(k,2)/(3*step_y)-2*theta(k,1)/(3*
      step_z)+c;
denominator4(k)=-2*theta(k,2)/(3*step_y)+2*theta(k,1)/(3*
      step_z)+c;

      if theta(k,1)>0 && theta(k,2)>0

      % % case   1
      for i=1:I
      for j=1:J
      for n=1:K
     sum1(n)=radiance(i,j,n)* w(k,n);
      end

      if (i==1)
         deriv_i=0;

       elseif (i==2)
            deriv_i=radiance(i-1,j,k);
       else
           deriv_i=radiance(i-1,j,k)+radiance(i-2,j,k);
       end

       if (j==1)
          deriv_j=0;
       elseif (j==2)
            deriv_j=radiance(i,j-1,k);
       else
           deriv_j=radiance(i,j-1,k)+radiance(i,j-2,k);
```

```
    end
numerator(i,j,k)=
     sum(sum1)*b+(deriv_i)*(theta(k,2)/(3*step_y))+(
     deriv_j)*(theta(k,1)/(3*step_z))+c*q(i,j,k);
radiance_temp(i,j,k)=numerator(i,j,k)/denominator1(k);
 end
 end

 elseif theta(k,1)<0 && theta(k,2)>0
 % % case   2

 for i=1:I
 for j=1:J

 for n=1:K
sum1(n)=radiance(i,j,n)* w(k,n);
 end

 if (i==1)
    deriv_i=0;
 elseif (i==2)
      deriv_i=radiance(i-1,j,k);
 else
     deriv_i=radiance(i-1,j,k)+radiance(i-2,j,k);
 end

 if (j==J)
    deriv_j=0;
 elseif (j==J-1)
      deriv_j=radiance(i,j+1,k);
 else
     deriv_j=radiance(i,j+1,k)+radiance(i,j+2,k);
 end


numerator(i,j,k)=
     sum(sum1)*b+(deriv_i)*(theta(k,2)/(3*step_y))-(
     deriv_j)*(theta(k,1)/(3*step_z))+c*q(i,j,k);

radiance_temp(i,j,k)=numerator(i,j,k)/denominator2(k);
 end
 end
 elseif theta(k,1)<0 && theta(k,2)<0
 % % case   3
 for i=1:I
 for j=1:J
 for n=1:K
sum1(n)=radiance(i,j,n)* w(k,n);

 end

 if (i==I)
    deriv_i=0;
 elseif (i==I-1)
      deriv_i=radiance(i+1,j,k);
 else
     deriv_i=radiance(i+1,j,k)+radiance(i+2,j,k);
 end

 if (j==J)
    deriv_j=0;
 elseif (j==J-1)
      deriv_j=radiance(i,j+1,k);
 else
     deriv_j=radiance(i,j+1,k)+radiance(i,j+2,k);
 end


numerator(i,j,k)=
     sum(sum1)*b-(deriv_i)*(theta(k,2)/(3*step_y))-(
     deriv_j)*(theta(k,1)/(3*step_z))+c*q(i,j,k);

radiance_temp(i,j,k)=numerator(i,j,k)/denominator3(k);
 end
 end
 else
 % % case   4

 for i=1:I
 for j=1:J
 for n=1:K
sum1(n)=radiance(i,j,n)* w(k,n);
 end

 if (i==I)
    deriv_i=0;
 elseif (i==I-1)
      deriv_i=radiance(i+1,j,k);
 else
     deriv_i=radiance(i+1,j,k)+radiance(i+2,j,k);
 end

 if (j==1)
    deriv_j=0;
 elseif (j==2)
      deriv_j=radiance(i,j-1,k);
 else
     deriv_j=radiance(i,j-1,k)+radiance(i,j-2,k);
 end

numerator(i,j,k)=
     sum(sum1)*b-(deriv_i)*(theta(k,2)/(3*step_y))+(
     deriv_j)*(theta(k,1)/(3*step_z))+c*q(i,j,k);

radiance_temp(i,j,k)=numerator(i,j,k)/denominator4(k);
 end
 end
 end
 end
radiance=radiance_temp;
 end

y=radiance;
```

this regard so as to make UOWC more reliable, namely: channel coding techniques, multi-hop relay-based UOWC, as well as laser and aperture diversity by leveraging optical multiple-input-multiple-output (MIMO) setups. On the other hand, the underwater link presents other impairments such as pointing error loss and turbulence induced fading, which should also be included in the overall UOWC channel modeling. The evaluation of UOWC path-loss is of paramount importance for quantifying the system's link budget which is very useful in the design of futuristic UOWC systems. Such systems can enable the deployment of various high-speed applications, such as underwater disaster recovery, military applications, and oil monitoring.

A potential extension of this work is considering the turbulence effects due to the dynamic change of the pressure and temperature in the marine medium, as well as taking into account the pointing error impairment.

APPENDIX
MATLAB CODE FOR THE PROPOSED RTE SOLVER

See Algorithm.

REFERENCES

[1] L. Johnson, R. Green, and M. Leeson, "A survey of channel models for underwater optical wireless communication," in *Proc. 2nd Int. Workshop Opt. Wireless Commun. (IWOW)*, Oct. 2013, pp. 1–5.

[2] Z. Zeng, S. Fu, H. Zhang, Y. Dong, and J. Cheng, "A survey of underwater optical wireless communications," *IEEE Commun. Surveys Tuts.*, vol. 19, no. 1, pp. 204–238, 1st Quart., 2017.

[3] E. Illi, F. E. Bouanani, D. B. da Costa, F. Ayoub, and U. S. Dias, "Dual-hop mixed RF-UOW communication system: A PHY security analysis," *IEEE Access*, vol. 6, pp. 55345–55360, 2018.

[4] H. Kaushal and G. Kaddoum, "Underwater optical wireless communication," *IEEE Access*, vol. 4, pp. 1518–1547, 2016.

[5] N. Saeed, A. Celik, T. Y. Al-Naffouri, and M.-S. Alouini, "Underwater optical wireless communications, networking, and localization: A survey," *Ad Hoc Netw. J.*, vol. 94, Nov. 2019.

[6] S. Arnon, J. Barry, G. Karagiannidis, R. Schober, and M. Uysal, *Advanced Optical Wireless Communication Systems*. Cambridge, U.K.: Cambridge Univ. Press, 2012.

[7] Z. Ghassemlooy, W. Popoola, and S. Rajbhandari, *Optical Wireless Communications: System and Channel Modelling with MATLAB*. Boca Raton, FL, USA: CRC Press, 2013.

[8] M.-A. Khalighi, C. Gabriel, T. Hamza, S. Bourennane, and P. Léon, and V. Rigaud, "Underwater wireless optical communication; recent advances and remaining challenges," in *Proc. 16th Int. Conf. Trans. Opt. Netw. (ICTON)*, Jul. 2014, pp. 1–4.

[9] C. Mobley, E. Boss, and C. Roesler. (2010). *Ocean Optics Web Book*. [Online]. Available: http://www.oceanopticsbook.info/

[10] C. Li, K.-H. Park, and M.-S. Alouini, "On the use of a direct radiative transfer equation solver for path loss calculation in underwater optical wireless channels," *IEEE Wireless Commun. Lett.*, vol. 4, no. 5, pp. 561–564, Oct. 2015.
[11] W. C. Cox, Jr., "Simulation, modeling, and design of underwater optical communication systems," Ph.D. dissertation, Dept. Elect. Eng., North Carolina State Univ., Raleigh, NC, USA, Feb. 2012.
[12] A. Kammoun, Z. Jiusi, B. S. Ooi, and M.-S. Alouini, "Impact of wavelength on the path-loss of turbid underwater communication systems," in *Proc. IEEE Wireless Commun. Netw. Conf. (WCNC)*, Apr. 2019, pp. 1–6.
[13] J. Ripoll, "Derivation of the scalar radiative transfer equation from energy conservation of Maxwell's equations in the far field," *J. Opt. Soc. Amer. A, Opt. Image Sci.*, vol. 28, no. 8, pp. 1765–1775, Aug. 2011.
[14] A. D. Klose and A. H. Hielscher, "Iterative reconstruction scheme for optical tomography based on the equation of radiative transfer," *Med. Phys. J.*, vol. 26, no. 8, pp. 1698–1707, Aug. 1999.
[15] H. Gao and H. Zhao, "A fast-forward solver of radiative transfer equation," *Transp. Theory Stat. Phys.*, vol. 38, no. 3, pp. 149–192, Sep. 2009.
[16] E. Illi, F. El Bouanani, and F. Ayoub, "A high accuracy solver for RTE in underwater optical communication path loss prediction," in *Proc. Int. Conf. Adv. Commun. Technol. Netw. (CommNet)*, Apr. 2018, pp. 1–8.
[17] S. Lloyd, "Least squares quantization in PCM," *IEEE Trans. Inf. Theory*, vol. 28, no. 2, pp. 129–137, Mar. 1982.
[18] E. Illi, F. El Bouanani, and F. Ayoub. (2019). *Numerical-RTE-Solver*. [Online]. Available: https://github.com/NumericalRTESolver/RTE-Solver
[19] S. K. Sahu and P. Shanmugam, "A theoretical study on the impact of particle scattering on the channel characteristics of underwater optical communication system," *Opt. Commun.*, vol. 408, pp. 3–14, Feb. 2018.
[20] C. D. Mobley, L. K. Sundman, and E. Boss, "Phase function effects on oceanic light fields," *Appl. Opt.*, vol. 41, no. 6, pp. 1035–1050, 2002.
[21] G. R. Fournier and J. L. Forand, "Analytic phase function for ocean water," *Proc. SPIE*, vol. 2258, Oct. 1994, pp. 194–201.
[22] V. I. Haltrin, "An analytic Fournier-Forand scattering phase function as an alternative to the Henyey-Greenstein phase function in hydrologic optics," in *Proc. Int. Geosci. Remote Sens. Symp. (IGARSS)*, vol. 2, Jul. 1998, pp. 910–912.
[23] M. Abramowitz and I. A. Stegun, *Handbook of Mathematical Functions With Formulas, Graphs, and Mathematical Tables*, 10th ed. New York, NY, USA: Dover, 1972.
[24] D. Anguita, D. Brizzolara, G. Parodi, and Q. Hu, "Optical wireless underwater communication for AUV: Preliminary simulation and experimental results," in *Proc. OCEANS IEEE Spain*, Jun. 2011, pp. 1–5.
[25] M.-K. Simon and M.-S. Alouini, *Digital Communication Over Fading Channels*. New York, NY, USA: Wiley, 2005.

ELMEHDI ILLI (S'19) was born in Rabat, Morocco, in 1992. He received the B.Sc. and M.Sc. degrees in computer sciences, telecommunications, and electrical engineering from the Faculty of Sciences, Mohammed V University, Rabat, in 2013 and 2015, respectively, where he is currently pursuing the Ph.D. degree with the ENSIAS College of Engineering. He has authored around eight publications in well-known conferences and journals, such as WINCOM, IWCMC, GLOBECOM, IEEE Access, and the IEEE Transactions on Sustainable Computing. His main research interests include the performance analysis and the design of wireless communication systems, particularly optical-based communications, underwater optical communications, signal processing, information theory, and physical layer security.

FAISSAL EL BOUANANI was born in Nador, Morocco, in 1974. He received the M.S. and Ph.D. degrees in network and communication engineering from Mohammed V University at Souissi, Rabat, Morocco, in 2004 and 2009, respectively.

He has served as a Faculty Member with the University of Moulay Ismail, Meknes, from 1997 to 2009, before joining the National High School of IT/ENSIAS College of Engineering, Mohammed V University, Rabat, in 2009, where he is currently an Associate Professor. He advised many Ph.D. and master's students at both Mohammed V and Moulay Ismail Universities. So far, his research efforts have culminated in more than 50 papers in a wide variety of international conferences and journals, including the IEEE Transactions on Communications, IEEE Access, the IEEE Wireless Communications Letters, the IEEE Transactions on Sustainable Computing, *Eurasip Journal on Wireless Communications and Networking*, *International Journal of Communication Systems* (Wiley), *Physical Communication* journal, PIMRC, GLOBECOM, IWCMC, and CROWNCOM. His current research interests include coding, cryptography, and performance analysis of wireless communication systems. He has also been involved as a TPC Member in various conferences, including VTC, ISWCS, IWCMC, UNET, and WinCom. His Ph.D. thesis was awarded the best one by Mohammed V University at Souissi, in 2010. He served as the TPC Chair of the ICSDE conferences and the General Co-Chair of ACOSIS'16 and CommNet'18 conferences. He serves currently as the General Chair of the 2019 CommNet conference and a Reviewer for the IEEE Communications Letters and the IEEE Transactions on Cognitive Communications and Networking.

KI-HONG PARK (S'06–M'11) received the B.Sc. degree in electrical, electronic, and radio engineering from Korea University, Seoul, South Korea, in 2005, and the joint M.S. and Ph.D. degrees from the School of Electrical Engineering, Korea University, in 2011. In April 2011, he joined KAUST as a Postdoctoral Fellow. Since December 2014, he has been a Research Scientist of electrical engineering with the Division of Computer, Electrical, Mathematical Science and Engineering (CEMSE), King Abdullah University of Science and Technology (KAUST), Thuwal, Saudi Arabia. His research interests include the broad field of communication theory and its application to the design and performance evaluation of wireless communication systems and networks. His current research interests include the application to underwater visible light communication, optical wireless communications, unmanned aerial vehicle communication, and physical layer secrecy.

FOUAD AYOUB was born in Kenitra, Morocco, in 1979. He received the B.Sc. degree in applied physics and the M.Sc. and Ph.D. degrees in engineering, telecommunications, and multimedia from the Faculty of Sciences, Mohammed V University, Rabat, Morocco, in 2002, 2005, and 2011, respectively.

From 2012 to 2016, he was an Assistant Professor with CRMEF, Morocco, where he is currently an Associate Professor. He advised the Ph.D. and master's students at both Mohammed V and Ibn Tofail Universities. So far, his research efforts have culminated papers in a wide variety of international conferences and journals including the IEEE Transactions on Communications, IEEE Access, the IEEE Transactions on Sustainable Computing, IWCMC, Commnet, and Globecom. His current research interests include telecommunications, information and coding theory, and performance analysis of wireless communication systems.

Dr. Ayoub was the General Co-Chair of the CommNet'19 Conference and the General Chair of the ICSDE'18 Workshop and the chair registration and publications of the ACOSIS'16 and CommNet'18 conferences . He has served as a reviewer for many international journals

MOHAMED-SLIM ALOUINI (S'94–M'98–SM'03–F'09) was born in Tunis, Tunisia. He received the Ph.D. degree in electrical engineering from the California Institute of Technology (Caltech), Pasadena, CA, USA, in 1998. He was a Faculty Member with the University of Minnesota, Minneapolis, MN, USA, and the Texas A&M University at Qatar, Doha, Qatar, before joining the King Abdullah University of Science and Technology (KAUST), Thuwal, Saudi Arabia, as a Professor of electrical engineering, in 2009. His current research interests include the modeling, design, and performance analysis of wireless communication systems.